Red, redder, reddest: SCUBA-2 imaging of colour-selected *Herschel* sources

S. Duivenvoorden,[1][*] S. Oliver,[1] J. M. Scudder,[1] J. Greenslade,[2] D. A. Riechers,[3] S. M. Wilkins,[1] V. Buat,[4] S. C. Chapman,[5] D. L. Clements,[2] A. Cooray,[6] K. E. K. Coppin,[7] H. Dannerbauer,[8,9] G. De Zotti,[10] J. S. Dunlop,[11] S. A. Eales,[12] A. Efstathiou,[13] D. Farrah,[14] J. E. Geach,[7] W. S. Holland,[11,15] P. D. Hurley,[1] R. J. Ivison,[11,16] L. Marchetti,[17,18,19] G. Petitpas,[20] M. T. Sargent,[1] D. Scott,[21] M. Symeonidis,[22] M. Vaccari,[18,19] J. D. Vieira,[23] L. Wang,[24,25] J. Wardlow[26] and M. Zemcov[27]

Affiliations are listed at the end of the paper

ABSTRACT

High-redshift, luminous, dusty star-forming galaxies (DSFGs) constrain the extremity of galaxy formation theories. The most extreme are discovered through follow-up on candidates in large area surveys. Here, we present extensive 850 μm SCUBA-2 follow-up observations of 188 red DSFG candidates from the *Herschel* Multitiered Extragalactic Survey (HerMES) Large Mode Survey, covering 274 $\deg^2$. We detected 87 per cent with a signal-to-noise ratio >3 at 850 μm. We introduce a new method for incorporating the confusion noise in our spectral energy distribution fitting by sampling correlated flux density fluctuations from a confusion limited map. The new 850 μm data provide a better constraint on the photometric redshifts of the candidates, with photometric redshift errors decreasing from $\sigma_z/(1 + z) \approx 0.21$ to 0.15. Comparison spectroscopic redshifts also found little bias ($\langle(z - z_{\rm spec})/(1 + z_{\rm spec})\rangle = 0.08$). The mean photometric redshift is found to be 3.6 with a dispersion of 0.4 and we identify 21 DSFGs with a high probability of lying at $z > 4$. After simulating our selection effects we find number counts are consistent with phenomenological galaxy evolution models. There is a statistically significant excess of *WISE*-1 and SDSS sources near our red galaxies, giving a strong indication that lensing may explain some of the apparently extreme objects. Nevertheless, our sample includes examples of galaxies with the highest star formation rates in the Universe ($\gg 10^3$ $M_\odot$ yr^{-1}).

Key words: galaxies: high-redshift – galaxies: starburst – Infrared: galaxies – submillimetre: galaxies.

1 INTRODUCTION

Over the last few decades, great progress has been made in understanding the star formation history of the Universe (see e.g. review by Madau & Dickinson 2014). It has become apparent that observing at UV and optical wavelengths is insufficient as a large fraction of the star formation is obscured, resulting in dusty starforming galaxies (DSFGs; see e.g. reviews by Lonsdale, Persson & Matthews 1984; Cesarsky et al. 1996; Smail, Ivison & Blain 1997; Burgarella et al. 2013; Casey, Narayanan & Cooray 2014). The most extreme forms of obscured star formation at high redshift still pose serious challenges to galaxy evolution models (e.g. Baugh et al. 2005; Lacey et al. 2010; Narayanan et al. 2010; Hayward et al. 2013; Béthermin et al. 2017). The discovery and characterization of the rarest and most extreme galaxies (star formation rates, SFR, $\gg 10^3$ $M_\odot$ yr^{-1}, number densities $\ll 10^{-4}$ Mpc^{-3}, Gruppioni et al. 2013) is thus an important goal, but requires large volume surveys at long wavelengths.

This is now possible with deep large-area surveys ($\gg 10\,\deg^2$) at far-infrared (FIR) and sub-mm wavelengths with e.g. the South Pole Telescope (SPT; Carlstrom et al. 2011) and the *Herschel Space Observatory* (Pilbratt et al. 2010).

Follow-up of SPT sources has been very successful in finding high-redshift DSFGs (Vieira et al. 2013; Weiß et al. 2013; Strandet et al. 2016, 2017). The SPT source selection at a wavelength of

[*] E-mail: S.Duivenvoorden@Sussex.ac.uk

1.4 mm has however a broader redshift distribution than *Herschel* detected sources (Greve et al. 2012).

Herschel surveys cover a huge area ∼1300 deg² (the largest being HerMES Oliver et al. 2012 and *H*-ATLAS Eales et al. 2010) and while most detections are associated with $z \sim 1$–2 starburst galaxies (e.g. Casey et al. 2012a,b) it has been clearly demonstrated that selecting those with red colours is extremely efficient for identifying a tail extending towards higher redshift ($z > 4$) (Cox et al. 2011; Riechers et al. 2013; Dowell et al. 2014; Asboth et al. 2016; Ivison et al. 2016; Donevski et al. 2017; Riechers et al. 2017; Zavala et al. 2018). The challenge now is using these very large *Herschel* surveys to find and systematically study, large, homogeneous samples of rare, extremely luminous, $z > 4$ sources.

Asboth et al. (2016) probed this high-redshift population in the largest *Herschel* Multitiered Extragalactic Survey (HerMES) field, the HerMES Large Mode Survey (HeLMS, covering approximately 300 deg²) by selecting all bright '500 μm riser' ($S_{500} > S_{350} > S_{250}$) DSFGs candidates. This sample was selected over an area a factor of 13 times larger than previous 500 μm riser HerMES surveys (Dowell et al. 2014). The number of sources that fulfilled these criteria (477) is an order of magnitude higher than predicted by galaxy evolution models (Béthermin et al. 2011, 2012; Dowell et al. 2014)

Another large 600 deg² red DSFGs search in the *H*-ATLAS survey (Ivison et al. 2016) used a 3.5σ (30 mJy) detection threshold at S_{500} in combination with $S_{500}/S_{250} \geq 1.5$ and $S_{500}/S_{350} \geq 0.85$ colour selection criteria to obtain a sample of 7961 candidate high-redshift DSFGs. After a visual inspection (Ivison et al. 2016) a sub-sample of 109 DSFGs, candidates were selected for follow-up at longer wavelengths with SCUBA-2 or LABOCA.

All these red sources are candidates for high-luminosity sources. Some, particularly those with a flux density at $S_{500} > 100$ mJy, are likely to be strongly gravitationally lensed (Negrello et al. 2010; Conley et al. 2011; Nayyeri et al. 2016; Negrello et al. 2017) others may be blends (e.g. Scudder et al. 2016). Nevertheless, they are extremely interesting because, those that are not lensed, blended, or otherwise boosted may represent the most active galaxies in cosmic history.

In this work, we present a follow-up study of 188 of the brightest 200 ($S_{500} > 63$ mJy), of the 477 Asboth et al. (2016) objects using SCUBA-2 (Holland et al. 2013) on the James Clerk Maxwell Telescope (JCMT). With the addition of the S_{850} data provided by SCUBA-2 we have a better constraint on both the FIR luminosities and the redshifts of these DSFGs and prepare the way for high-resolution follow-up.

With our sample of 188 galaxies observed by SCUBA-2 we roughly double the number of 500 μm riser galaxies possessing longer sub-mm wavelength data.

The format of this paper is as follows. We describe the data in Section 2. We describe our methods for determining the photometric redshifts, FIR luminosities and SFRs in Section 3. The results are described in Section 4, and the discussion and conclusions in Sections 5 and 6, respectively. We use a standard flat cosmology with $\Omega_M = 0.3$ and $H_0 = 70$ kms⁻¹Mpc⁻¹.

2 DATA

2.1 Selecting high-redshift dusty galaxies in HeLMS

We use the red HeLMS sample identified in Asboth et al. (2016) and below follows a short summary of their selection. The area mapped by HeLMS is a 300 deg² equatorial field which is part of the HerMES project. The observations were performed using the SPIRE instrument (Griffin et al. 2010) on board the *Herschel Space Observatory*. Some parts of the HeLMS field were masked. Edge effects, along with a 'seagull-shaped' region of strong Galactic cirrus were removed, leaving a useful area of 274 deg².

Sources were detected using a map-based search method described in Asboth et al. (2016), similar to what was used in Dowell et al. (2014), instead of sources from the HerMES catalogue derived directly from the 250 μm map (Clarke et al., in preparation). For a description of how the sources were selected and the exact spatial filters adopted we refer the reader to Asboth et al. (2016), but we give a brief description here for completeness.

The SPIRE 250, 350, 500 μm maps are created with the same pixel size (6 arcsec) and (for source detection only) smoothed to the same resolution using an optimal filter for easy comparison between wavebands (Chapin et al. 2011). The local background is removed by smoothing the maps with a 2D median boxcar filter on 3 arcmin scales to remove any cirrus contamination. The filters are also applied to the error map to find the typical instrumental noise in the smoothed map. The 1σ instrumental noise values are 7.56, 6.33, and 7.77 mJy, in the 250, 350, and 500 μm SPIRE bands.

The confusion noise (σ_{conf}) in the SPIRE map is caused by sources which emit at all three SPIRE wavelengths. This causes the confusion noise to be correlated between wavelengths. This information is used to construct a difference map (D) from the SPIRE 500 μm (M_{500}) and SPIRE 250 μm (M_{250}) maps with a reduced confusion limit (Dowell et al. 2014);

$$D = \sqrt{1 - k^2} M_{500} - k M_{250} \qquad (1)$$

with a k value of 0.392 to maximize the D/σ_{conf}. This D-map has a confusion noise of 3.50 mJy, which is much lower than in the three smoothed SPIRE bands (13.66, 11.21, 6.98 mJy at 250, 350, and 500 μm, respectively).

The bright peaks in the D-map are selected with a 4σ cut-off at 34 mJy. At these positions the SPIRE flux densities are determined from the (higher resolution) nominal resolution map while taking into account the positional uncertainty of 6 arcsec (as measured with simulations in Asboth et al. 2016). From these flux densities a catalogue of $S_{500} > S_{350} > S_{250}$ sources is created. There is no requirement for a detection in both 250 and 350 μm, in order to avoid biasing the selection against the reddest objects.

The smoothed and raw images are compared with each other within a 30 × 30 arcsec region around each source to find cosmic rays. All candidate sources with $S_{raw} - S_{smooth} > 5\sigma_{raw}$ are removed. The final catalogue is selected to have $S_{500} > 52$ mJy in order to minimize the effect of faint cosmic rays which are not found by the described technique. All 17 sources with radio fluxes in excess of 1 mJy are removed using the 21 cm radio catalogues from the NRAO VLA Sky Survey (NVSS, Becker, White & Helfand 1995) and the Radio Sky at Twenty-cm (FIRST) survey (Condon et al. 1998) to avoid contamination by flat spectrum quasars at $z < 1$. The rejection of NVSS/FIRST sources means that we potentially miss some genuine red sources that are lensed by radio-loud galaxies (Haas et al. 2014; Leung & Riechers 2016). The final Asboth et al. (2016) catalogue contains a total of 477 sources.

2.2 SCUBA-2

We selected the 200 brightest galaxies i.e. $S_{500} > 63$ mJy, of the 477 Asboth et al. (2016) sources, and we observed a random sub-set of 188 of them for 15 min each using the DAISY pattern with the SCUBA-2 camera at the JCMT (Holland et al. 2013). The observations were taken in semester 15B between 2015 July 31

and 2015 November 15 with an opacity at 225 GHz between 0.05 and 0.12.

Our integration times were based on the previous observations of 28 red objects from Dowell et al. (2014) with almost identical selection criteria as our sample. Those observations were 12. 5 min `DAISY` observations and 27 out of the 28 where detected. Using the S_{850}/S_{500} colour distribution from these data to simulate the 850 µm fluxes of the HeLMS sample we estimated that a 1σ rms$_{850}$ = 4.5 mJy would detect 70 per cent of our targets at $>3\sigma$.

We explored several data reduction methods including the data reduction used for the SCUBA-2 Cosmology Legacy Survey (S2CLS; Geach et al. 2017), and the quick pipeline reduction using `REDUCE SCAN FAINT POINT SOURCES`. We found that the 'zero-mask' (Holland et al. 2017) data reduction used in Ivison et al. (2016) provided us with the highest signal-to-noise values and a rms$_{850}$ ranging between 3.2 and 6.4 mJy with a mean of 4.3 mJy where the S2CLS method reaches an average rms$_{850}$ of 4.9 mJy. The flux densities obtained with the zero-mask method are on average 2.6 ± 4.0 mJy higher than the S2CLS method. We decided to use the zero-mask data reduction technique for all our observations because of its effectiveness in suppressing large-scale noise (Ivison et al. 2016; Holland et al. 2017).

The zero-mask data reduction uses the Dynamic Iterative Map Maker within the SMURF package (Chapin et al. 2013). This algorithm assumes that the image is free of significant emission except for a 60 arcsec diameter region centred on our target. Since the positions of our targets are in the centres of our `DAISY` observations this algorithm is very effective in suppressing large-scale noise. This has an advantage over the S2CLS pipeline (Geach et al. 2017), which can make no prior assumptions about the positions of the targets. The maps are generated with 1 arcsec × 1 arcsec pixels.

We use the same data reduction technique for the SCUBA-2 flux calibrators to get accurate flux conversion factors (FCF). These FCFs, ranging between 658 and 777 Jy pW^{-1} beam^{-1}, are used to convert our reduced image to units of Jy beam^{-1}. The FCFs are expected to be accurate to within 5 per cent (Dempsey et al. 2013).

Our prior positions are derived from the *Herschel* data and have a typical positional uncertainty (σ_H) of 6 arcsec (Asboth et al. 2016). Another positional uncertainty arises from the JCMT 2–3 arcsec rms pointing accuracy (σ_J). We combine both uncertainties to obtain the final positional uncertainty (σ_p):

$$\sigma_p = \sqrt{\sigma_H^2 + \sigma_J^2}. \tag{2}$$

We apply our source extraction by taking the flux density of the brightest pixel within a 20 arcsec radius of our prior position in the beam convolved image. This 20 arcsec radius corresponds roughly to the $3\sigma_p$ positional uncertainty of our prior source in the SCUBA-2 map. We obtained an average noise level of 4.3 mJy for our point source extraction.

For the purpose of analysis we divide our sample into three sub-groups with fairly arbitrary signal-to-noise ratio boundaries. Group 1 contains objects that have a clear detection, $S_{850} \geq 5\sigma$. Group 2 consists of detections between $3\sigma \leq S_{850} < 5\sigma$. Finally, Group 3 are galaxies for which we do not have a clear detection, $S_{850} < 3\sigma$. (Due to the large uncertainty in position we are unable to obtain a significant detection in the stacked signal for the Group 3 galaxies.) The three groups contain 64, 99, and 25 objects, respectively.

As we are considering SCUBA-2 measurements of *Herschel* detected galaxies we are concerned about the accuracy of the flux measurement, rather than the reality of a catalogued source (as we
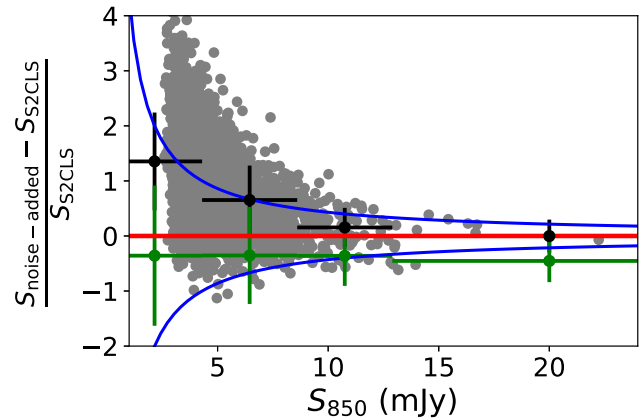
Figure 1. Simulation of our photometric errors and biases. S2CLS maps and catalogues are taken to be the truth and the noise-added fluxes are generated by adding Gaussian noise to mimic our observations ($\sigma = 4.3$ mJy). Flux densities are measured by taking the highest flux density within a 20 arcsec radius from the new S2CLS source position. The new S2CLS positions are generated by adding a random positional error of $\sigma = 7$ arcsec to it, which is comparable with the positional error of our data. The fractional difference between the (S2CLS) 850 µm flux density 'truth' and the measured 850 µm flux density are plotted as function of the S2CLS flux density for all sources in grey, the black points show the mean of this measured fraction and the green points show the mean for a nearest pixel source extraction. The red line indicates zero offset and the blue lines indicate 1σ (4.3 mJy) bounds.

would be with a blank field survey). Nevertheless we would expect random noise fluctuations and confusion noise from galaxies not associated with our original target. Furthermore, we are using the brightest pixel, so our flux measurements are biased high (Coppin et al. 2008). We quantify this bias using the simulation shown in Fig. 1. This simulation takes all deep S2CLS fields as the 'truth'.

We add noise to the S2CLS maps by adding extra Gaussian noise to reach a total noise of $\sigma = 4.3$ mJy, similar to those of our observations, we call this new maps the noise-added map. We then add positional errors to the S2CLS catalogue with a mean of zero and a standard deviation of 7 arcsec to the S2CLS positions to simulate the positional uncertainty of our DSFGs. We then apply our photometric measurement at the original S2CLS position and compare with the original S2CLS flux. We repeat this process five times to get the results from different random noise simulations.

The comparison shows that for sources with S_{850} below 13 mJy (3σ) we are (on average) overestimating the flux density, but this overestimation is on average lower than 4.3 mJy (1σ). We also tested the sources extraction method of picking the nearest pixel to our prior positions and find that this method underestimates the flux density significantly for sources with $S_{850} > 13$ mJy. We decided to use our brightest pixel sources extraction because we expect that a significant percentage of our sources will lie above $S_{850} > 13$ mJy given that $S_{500} > 63$ mJy.

2.3 Ancillary data

It is unlikely that our high-redshift galaxy sample will be directly detected in any shallow large-field surveys at optical/NIR wavelengths which are not likely to contain $z > 1$ galaxies without an AGN (Section 4.2). However, low-redshift galaxies can significantly magnify a higher redshift source behind them via gravitational lensing.

Therefore, it is possible to identify a lens using the available low-redshift galaxies from the *Wide-field Infrared Survey Explorer* (Wright et al. 2010, *WISE*) and the Sloan Digital Sky Survey (York

et al. 2000, SDSS). We examined the SDSS images for possible contamination from large extended nearby galaxies and we found none. However, we do find several SDSS galaxies nearby and within the FWHM area of the SPIRE beam. Due to the large SPIRE/SCUBA-2 beam it will not be possible to unambiguously identify which of the several galaxies within the beam is potentially lensing the DSFG or is the optical/NIR counterpart of the DSFG.

For all our sources (excluding HELMS_RED_80 and HELMS_RED_421, see AGN Section 4.2) we find a total of 400 *WISE* detected sources (Cutri et al. 2013) within a 20 arcsec radius. Of those sources only one is detected ($>5\sigma$) in *WISE*-4 and this source is located 19.8 arcsec away from the SPIRE detection, additionally we find four *WISE*-3 detections ($>5\sigma$) near other sources which are all located >11.2 arcsec away from the SPIRE detection. For the numerous detections in the *WISE*-1 band it is not clear if the *WISE* source is a random aligned nearby galaxy, associated with our source, is an AGN or is lensing the background DSFG. We therefore did not use *WISE* data in our SED fit. We can, however, study the statistical excess of galaxies nearby to our sources (Wang et al. 2011), where we only use *WISE*-1 sources as all but two *WISE*-2 galaxies are detected in *WISE*-1. We use SDSS DR9 (Ahn et al. 2012) and the Cutri et al. (2013) *WISE* catalogue to select all detected galaxies near the line of sight of our targets (see Section 5.1).

Strong gravitational lensing, with a lensing magnification factor (μ) larger than 2, could provide an explanation for our high flux densities. Wide field *Herschel* surveys show that galaxies with a flux density at $S_{500} > 100$ mJy are likely to be strongly gravitationally lensed (Negrello et al. 2010; Conley et al. 2011; Nayyeri et al. 2016; Negrello et al. 2017). This $S_{500} > 100$ mJy limit comes from the steep slope in the FIR luminosity function, which causes intrinsically luminous ($S_{500} > 100$ mJy) sources to be extremely rare. Our sample of 500 μm riser galaxies contains nine galaxies with $S_{500} > 100$ mJy, of which we expect ≥ 80 per cent to be strongly lensed (Negrello et al. 2010; Wardlow et al. 2013). The probability that a DSFG is strongly lensed declines for $S_{500} < 100$ mJy, but for galaxies around 70 mJy at S_{500} there is still a significant (~ 20 per cent) chance that they are lensed (Bussmann et al. 2015; Nayyeri et al. 2016).

Other follow-up programs have observed part of our sample:

(i) Four of the sources (HELMS_RED_3, HELMS_RED_4, HELMS_RED_6, and HELMS_RED_7) were observed at the CSO using MUSIC (Sayers et al. 2014) at four wavelengths, 2.09, 1.4, 1.1, and 0.92 mm. The resulting flux densities can be found in section 6.2 and table 4 of Asboth et al. (2016).

(ii) Two sources (HELMS_RED_4, HELMS_RED_31) have spectroscopic follow up with the Atacama Large Millimeter Array (ALMA). The resulting spectra can be found in Asboth et al. (2016). The redshift of HELMS_RED_4 is 5.162 and the redshift of HELMS_RED_31 is 3.798 or 4.997 depending on the line detection being the CO(5–4) or the CO(4–3) line.

(iii) Two sources (HELMS_RED_1, HELMS_RED_2) have spectroscopic follow up by the Combined Array for Research in Millimeter-wave Astronomy (CARMA). The detected redshifts are 4.163 and 4.373, respectively (Riechers et al., in preparation; Leung et al., in preparation).

(iv) Five sources (HELMS_RED_1, 2, 4, 10, 13) have been observed with the Submillimeter Array (SMA), and will be discussed in detail in Greenslade et al. (in preparation).

(v) Two sources (HELMS_RED_1, 3) are detected in the Atacama Cosmology Telescope (ACT) equatorial survey (Su et al. 2017). The measured flux densities at 148, 218, and 278 GHz

are 12.49 ± 1.74, 35.11 ± 2.62, and 72.32 ± 6.26 mJy for HELMS_RED_1 and 6.14 ± 1.76, 19.50 ± 2.56, and 35.32 ± 6.24 mJy for HELMS_RED_3.

(vi) Twelve sources (HELMS_RED_3, 4, 7, 10, 19, 23, 31, 68, 69, 82, 118, 270) have 870 μm continuum observations from ALMA (Oteo et al. 2017b).

MUSIC and ACT provide even more data points in the Rayleigh−Jeans part of the spectrum. These additional long wavelength data will improve our SED-fitting process. The spectroscopic redshifts from CARMA and ALMA will be used to help validate our SED-fitting process and to confirm that our selection process does indeed pre-select high-redshift galaxies. We use the preliminary SMA results to get accurate information about the source positions and to determine if any sources are blended.

3 MODELING THE DSFGS

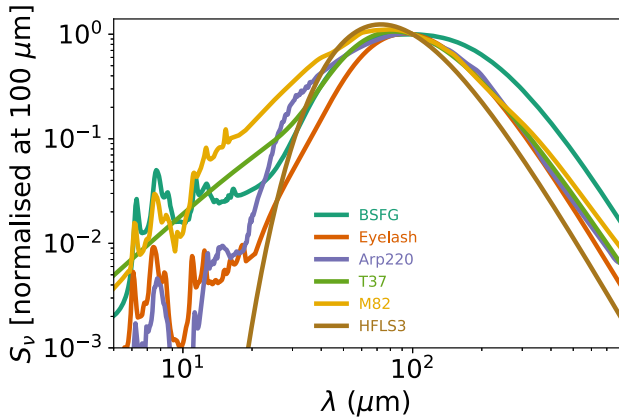### 3.1 Sed fitting for photometric redshifts

Fits to the FIR/sub-mm spectral energy distributions (SED) to obtain photometric redshifts and integrated properties are performed using the EAZY code (Brammer, van Dokkum & Coppi 2008) using a sample of representative FIR/sub-mm templates (e.g. Aretxaga et al. 2003).

The FIR peak of luminous infrared galaxies ($L_{IR} > 10^{10} L_{\odot}$) can be, crudely, characterized by cool dust with average temperatures in the 25–45 K range (e.g. Soifer et al. 1984; Klaas et al. 1997). The lack of strong features means it is difficult to distinguish between either very cold dust or high-redshift galaxies using only SPIRE photometry. The addition of the S_{850} data enables us to estimate the peak of the FIR emission, and therefore able to place far tighter constraints on the redshift (Section 3.3). However, since temperature and redshift are degenerate the choice of templates is a critical factor in photometric redshift estimation and so our templates have been carefully chosen to cover a broad range of temperatures.

Our six templates consist of the broad star-forming galaxy (BSFG) derived by Berta et al. (2013), cosmic Eyelash and three warm starburst galaxies M82, Arp220 (Polletta et al. 2007) and HFLS3 (Riechers et al. 2013). However, these templates have a gap at an effective temperature 37 K so we create an extra SED template from a modified blackbody (MBB) with a temperature of 37 K, a dust emissivity index (β) of 1.5 and a MIR power-law component (α) of 2.0 (Casey 2012). These templates are illustrated in Fig. 2. With EAZY we fit all possible linear combinations of our templates set.

In Fig. 3, we show the colour–colour plot of our observations. We overlay the redshift tracks from our sample of SED templates. Our template set thus contains a wide range of representative DSFGs over a large redshift range. We can exclude very cold ($T \sim 20$ K) galaxies at $z \lesssim 1.7$ as they would not be a 500 μm riser. Such galaxies at higher redshift could potentially contaminate our sample. But this type of galaxies are very rare between $0.1 < z < 2.0$ (Symeonidis et al. 2013). Such a cold galaxy would furthermore have a higher S_{850}/S_{500} colour than any of our measured S_{850}/S_{500} colours at $z > 2.5$.

We only use broad-band FIR data, and we neglect the contribution of emission lines. At redshifts of $z \sim 4$ FIR lines have a ~ 6 per cent effect at 250 μm, however, they have a negligible effect at 350, and 500 μm; at 850 μm they have a ~ 1 per cent contribution at $z \sim 4$ though this rises to ~ 8 per cent at $z \sim 5$ (Smail et al. 2011).

Figure 2. The six spectral energy distribution templates SEDs that we use in our photometric redshift fitting process. These are broad star-forming – BSFG derived by Berta et al. (2013), cosmic Eyelash, and three warm starburst galaxies M82, Arp220 (Polletta et al. 2007), and HFLS3 (Riechers et al. 2013).
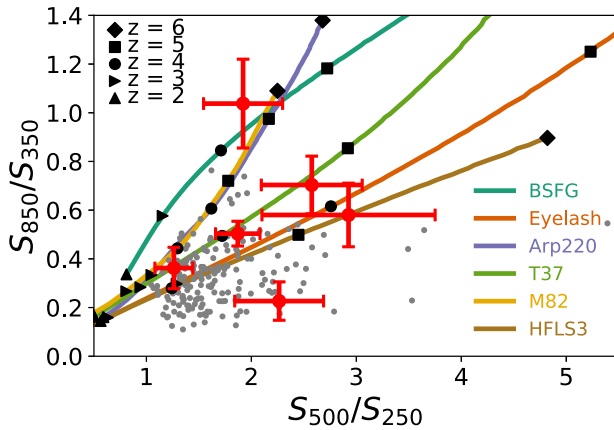

Figure 3. Colour–colour plot of our sample of DSFGs in grey, with a sub-set of points with representative error bars in red. The coloured lines show the redshift tracks of our SED templates. The crossing of such a line indicates that for a certain colour there are degenerate solutions for the photo-z estimates. The black shapes indicate the colour of a SED template at the indicated redshift. The data points significantly below the HFLS3 line could only be sampled by a non-physical template narrower than a blackbody. The presence of the DSFGs in this part of the diagram indicates flux boosting in either S_{350} or S_{500} (see Section 5).

We adjust EAZY to allow for 10 per cent systematic error for the data. This 10 per cent incorporates both the 5 per cent error in the FCF for SCUBA-2 and our use of a different algorithm to reduce the data for SCUBA-2 and SPIRE. The advantage of using this extra 10 per cent systematic error is that it dominates unrealistically small statistical errors for very bright ($>10\sigma$) sources.

In Section 3.4, we directly compare our method with other methods, other template choices and with spectroscopic redshifts.

3.2 Noise estimates

The SPIRE and SCUBA-2 maps contain both confusion and instrumental noise. Both have to be included in the SED fitting to ensure that the errors on fitted parameters, e.g. photometric redshift are assigned the appropriate errors. The confused background in the SPIRE band is caused by coincident sources; these contribute in all three wavelength bands. The instrumental noise can be assumed to
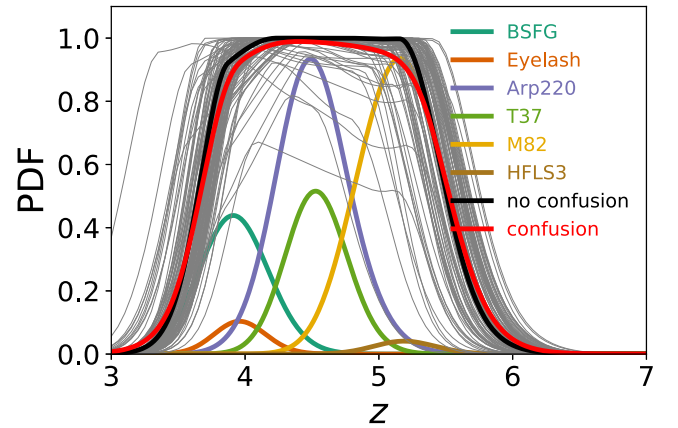
Figure 4. Redshift PDF for a single galaxy, illustrating the contribution from different galaxy templates. Each grey line represent the PDF from a single run with EAZY, perturbed by one particular sample of the confusion noise. The red line represents the average of the 1000 EAZY runs and the black line is the result from the traditional method without confusion noise. The coloured lines show the contribution to the PDF from each galaxy template used.

be uncorrelated and included straightforwardly in the χ^2 calculations within EAZY. However, to incorporate the confusion noise we need to consider that this is correlated noise.

The confusion noise at S_{850} from SCUBA-2 is significantly lower than the confusion in the SPIRE bands (1 mJy versus $\sim$6–7 mJy; Nguyen et al. 2010; Geach et al. 2017) due to the smaller beams size of SCUBA-2 and lower number counts. The SCUBA-2 confusion noise is subdominant to the instrumental noise we obtained in the images. We can therefore safely neglect the effects of confusion in our SCUBA-2 flux density estimates. We can simulate possible values for the SPIRE contribution in the following way.

In a confusion limited map, where the instrumental noise is negligible compared with the confusion noise, the fluctuations in that map can be considered to be caused by confusion noise alone. We can randomly sample such a confusion limited map at the same position in all three bands drawing a 3-tuple of flux density values that represent the confusion noise. These samples automatically include the correlation between the bands.[1]

The HELMS field is not confusion limited so we sample the confusion limited COSMOS (Scoville et al. 2007) field. COSMOS has a 1σ instrumental noise <2.5 mJy, though small, this residual instrumental noise means we will slightly overestimate the confusion noise values. We perturb the 3-tuple flux of each object in our catalogue by one of the sample 3-tuples drawn from COSMOS. We then run EAZY on the perturbed catalogue. We do this simulation exercise 1000 times (however, due to the finite size of the field these are not independent).

We average the redshift probability distribution function (PDF) over all simulation runs to obtain the final PDF for each galaxy. The results of 1000 runs for a single representative galaxy are shown in Fig. 4. The resulting PDF is slightly broader than the PDF from the traditional method of not using the confusion noise. This effect would be larger if the noise in HeLMS had been dominated by confusion noise.

---

[1] An alternative, would be to estimate the covariance matrix between the maps, and synthesize correlated flux density values from this assuming Gaussian fluctuations. However, by sampling directly from the map we skip this step and get a more direct model of the correlated confusion noise.
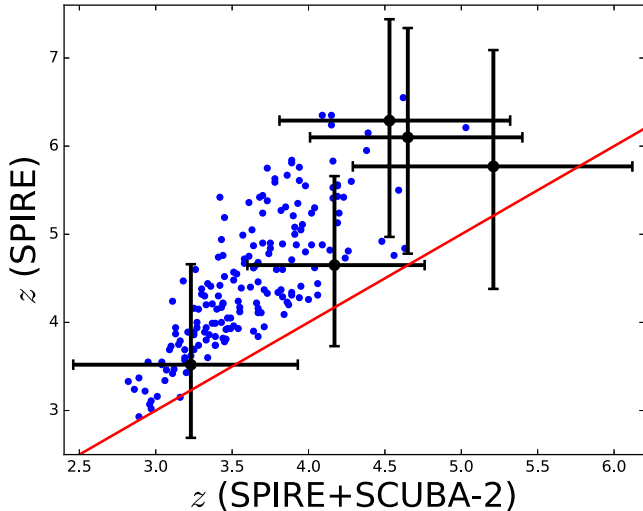
Figure 5. Redshift estimates from our SED fits using SPIRE photometry only versus those where we include SCUBA-2 data. All points in blue, and in black a subset of representative error bars. The average uncertainty for the SPIRE-only data set is larger, $\sigma_z/(1 + z) = 0.21$, than the uncertainty with the additional SCUBA-2 data $\sigma_z/(1 + z) = 0.15$. It is also clear that the SPIRE-only SED fits overestimate the redshift due to the lack of constraints on the peak of the FIR emission.

In Fig. 5, we show the improvement in photometric redshift by adding the longer wavelength SCUBA-2 data. The average uncertainty (calculated from the variance of the estimated PDF from EAZY) when we only use the SPIRE flux densities is larger, $\sigma_z/(1 + z) = 0.21$, than the uncertainty with the additional SCUBA-2 data $\sigma_z/(1 + z) = 0.15$. This figure also shows that we overestimate the photometric redshift when we only use the SPIRE data.

3.3 Physical parameters

Using EAZY we obtain the full PDF and the best-fitting SED template for every galaxy. With this template we compute the total infrared luminosity, L_{IR}. The FIR luminosity is defined as the integral over the rest-frame spectrum between 8 and 1000 μm, i.e. $L_{IR} = \int_{8\,\mu m}^{1000\,\mu m} L_\nu \, d\nu$. In practice, we lack a good measurement of the flux in the rest-frame mid-infrared (MIR) from 8 to 30 μm. We therefore integrate between 30 and 1000 μm and use a correction factor for the potentially large amounts of missed flux in the MIR. We calculate the correction factor from the average fraction of the FIR luminosity contained in the MIR regime for five of our six templates. We exclude the HFLS3 template for this measurement due to a lack of constraints in the MIR. We obtain a correction factor of 1.17 and we multiply our measured integral by this factor to obtain the resulting L_{IR}. We also obtain an error on L_{IR} using both the errors on our flux density estimates and the scatter from our 1000 EAZY runs.

The negative K-correction (for galaxies measured at longer wavelengths than the peak of their SED) counteracts (to some extent) the dimming with distance, and so these galaxies are relatively constant in brightness (e.g. Casey et al. 2014). Therefore, our estimates of L_{IR} can be tightly constrained even with a large uncertainty in the redshift.

Our L_{IR} can be translated into SFR estimates using Kennicutt (1998) for a Salpeter IMF

$$\frac{SFR}{M_\odot\,yr^{-1}} = 1.96 \times 10^{-10} \frac{L_{IR}}{L_\odot}. \tag{3}$$

Here, the fraction of ultraviolet energy absorbed by dust has been assumed to be $\epsilon = 0.88$, for which we have no constraint. Our estimates for the SFR would be the same if we had used the Rowan-Robinson et al. (1997) calibration factor with a $\epsilon = 2/3$. We assume no gravitational lensing (Section 5.1) and no contamination by AGN (Section 4.2) in our calculation of the SFR. The resulting SFRs should be multiplied by a factor 0.63 or 0.67 if assuming a Chabrier or Krupa IMF (Madau & Dickinson 2014).

Our final catalogue is presented in Appendix A, where we list the positions, flux densities, redshifts and L_{IR} of all our galaxies observed with SCUBA-2.

3.4 Testing the photometric redshifts

Ivison et al. (2016) made a similar assumption with the selection of their templates, and tested their photometric redshift code against 25 red high-redshift DSFGs with spectroscopic redshift. Their photometric redshifts where found by finding the lowest χ^2 value for their set of three templates. The main difference between our method is that EAZY not only fits the provided templates but also any linear combination of those templates. The results from Ivison et al. (2016) show only a small offset in $(z_{phot} - z_{spec})/(1 + z_{spec}) = -0.03$ with a scatter of 0.14.

We compare our photometric redshift method (z_{EAZY}) directly with Ivison et al. (2016), by running our code on their sample. We obtain a mean (μ) offset in $(z_{EAZY} - z_{Ivison})/(1 + z_{EAZY})$ of 0.11 and a median ($\mu_{1/2}$) offset of 0.12. We note that this offset is smaller than the mean estimated error in our redshift ($\langle \sigma_z/(1 + z_{EAZY}) \rangle = 0.15$).

The main difference between our method and that of Ivison et al. (2016) is that they tested a set of six templates individually with a sample of available spectroscopic redshifts, and discarded the ones with the poorest fit in $(z_{Ivison} - z_{spec})/(1 + z_{spec})$. Two of the poorest fitting templates in their analysis were the Arp 220 and HFLS3, which are on the 'blue' end of the range of FIR SEDs. If we discard our 'blue' templates (M82, HFLS3, and Arp 220) we find that our photometric redshift estimates are very close to the Ivison et al. (2016) estimates ($\mu = 0.024$ and $\mu_{1/2} = 0.035$). However, we keep these 'blue' templates in our analysis, to ensure conservative errors, noting that EAZY produces a full redshift PDF using all our templates (and all linear combinations of them) simultaneously.

We can see how our results would change if we made a different choice of templates. Strandet et al. (2016) used a Monte Carlo method to sample a range of MBB from Greve et al. (2012) with dust temperature parameter sampled from a Gaussian with mean and standard deviation 39 ± 10 K. We use a similar full MCMC approach to fit using the FITIR module of the INTERROGATOR[2] code (Wilkins et al., in preparation). With this method we can specify prior information about all free parameters. We consider both the MBB parametrization of Greve et al. (2012) (which has two free parameters, the temperature T, and the emissivity β) and the parametrization of Casey (2012) (which has three free parameters: the temperature, emissivity β, and the slope of the near-IR power-law α). For the Greve et al. (2012) parametrization we fix the emissivity $\beta = 2.0$ and consider three different priors on the temperature T: fixed to $T = 40$ K, a normal distribution centred at $T = 39$ K with $\sigma = 10$ K, and a uniform prior $T/K = [20, 40]$. For the Casey (2012) we assume uniform prior on the temperature of $T/K = [20, 60]$ and consider cases where both α and β are fixed (to 2.0 and 1.5, respectively) and where they have a uniform prior: $\beta = [1, 2]$ and $\alpha = [1., 2.5]$.

Table 1. Comparison of templates for photometric redshift accuracy. Mean photometric redshift, 1σ error, mean difference (μ) with the photometric redshift used in this work in $\frac{z-z_{\text{this work}}}{1+z_{\text{this work}}}$ and, the rms scatter (σ) in μ as function of different photometric redshift methods. The last row shows the sum of the χ^2 in comparison with the three spectroscopic redshifts of our sample. The Gaussian (39 ± 10 K) model produces comparable results compared to our method, but slightly overestimates the error bar size. The delta model is insufficient in fitting photometric redshifts, and the uniform models vastly overestimate the error bar size.

Method	This work	Gaussian (39 ± 10 K)	Uniform (20–60 K)	Delta (40 K)	Casey (20–60 K)	Casey wide (20–60 K)
$\langle z \rangle$	3.60 ± 0.43	3.34 ± 0.37	3.54 ± 0.40	3.24 ± 0.32	4.46 ± 0.54	4.79 ± 0.51
$\langle z_{\text{h}} - z_{\text{l}} \rangle / 2$	0.67	1.04	1.16	0.32	2.03	1.80
μ	0	-0.056	-0.011	-0.078	0.187	0.260
σ	0	0.034	0.041	0.027	0.043	0.033
χ^2	3.07	1.35	0.67	53.6	0.35	0.62
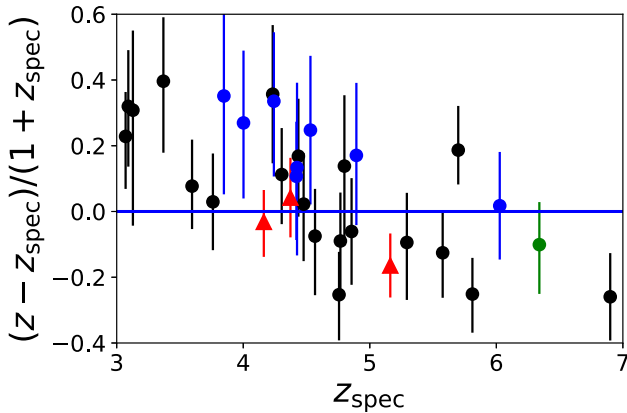
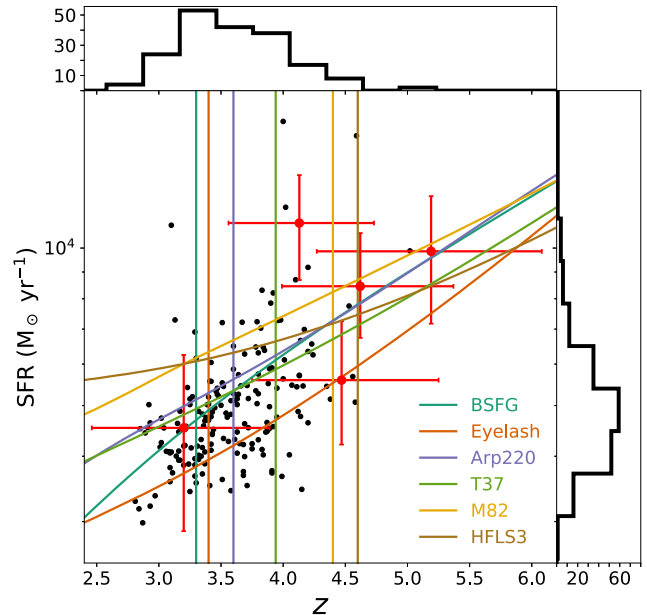**Figure 6.** Comparison with available 500 µm riser spectroscopic redshifts at $z > 3$. In green we show HFLS3, in black the SPT sample, and in blue the *H*-atlas sample (Weiß et al. 2013; Strandet et al. 2016, 2017; Fudamoto et al. 2017) and in red the spectroscopic redshifts for our sample. We obtain an offset $\langle (z - z_{\text{spec}})/(1 + z_{\text{spec}}) \rangle = 0.08$ with a rms of 0.19 and an average χ^2 per galaxy of 1.4.

Figure 7. SFR versus redshift for our 188 targets. Red represents a set of representative error bars. There are several objects which have a strong indication to lie at very high redshifts, but the bulk of our sample is expected to lie around $z \approx 3-4$. The coloured lines represent the lower redshift limits for 500 µm riser galaxies and SFR tracks for our range of SED templates.

The results are shown in Table 1 where we compare the output of each different template set to our chosen templates when applied to our sample. We compute a number of comparison statistics, the mean offset ($\mu = \frac{z-z_{\text{this work}}}{1+z_{\text{this work}}}$), the rms scatter in μ (σ) and the χ^2 in comparison with our three spectroscopic redshifts. For the normal distributed ($T = 39$ K) method we find a $\mu = -0.056$ and a $\chi^2 = 1.35$, for the uniform prior ($T/\text{K} = [20, 40]$) μ is -0.011 and the $\chi^2 = 0.67$ and for the single temperature model we find a $\chi^2 = 54$. From these results we can see that the Gaussian prior produces very similar results as our method, and that the flat 20–60 K prior models are consistent with the spectroscopic redshifts, but overestimate the size of the error bars ($\chi^2 \ll 1$). The single temperature model is insufficient in fitting photometric redshifts.

The ultimate test is the comparison against spectroscopic redshifts. We obtain a good total χ^2 of 3.07 for our three spectroscopic redshifts. But due to the limited number of spectroscopic redshifts in our sample we also use the SPT detected DSFGs which fulfil our colour selection criteria (Weiß et al. 2013; Strandet et al. 2016, 2017), HFLS3 and the *H*-atlas 500 µm risers Fudamoto et al. (2017). The results are shown in Fig. 6. We estimate a bias of $\langle (z - z_{\text{spec}})/(1 + z_{\text{spec}}) \rangle = 0.08$ with an rms of 0.19 and a reduced χ^2 of 1.4. The rms scatter in the bias (0.19), our average uncertainty per galaxy ($\sigma_z/(1 + z) = 0.15$) and $\langle |z - z_{\text{spec}}|/(1 + z_{\text{spec}}) \rangle = 0.17$ all have comparable values.

There is a visible trend in Fig. 6 that $(z - z_{\text{spec}})/(1 + z_{\text{spec}})$ is decreasing with redshift, the reduced χ^2 for linear decreasing model is 0.9 compared to 1.4 for the non-evolving model. This result in-

dicates that we underestimate the redshift of high-redshift galaxies due to a rising dust temperature of our spectroscopic sample towards higher redshift (Ivison et al. 2016). However, this same result could also arise from selection effects, where a warm HFLS3 type galaxy would not have made our selection criteria at $z < 4.6$ as it would not be a 500 µm riser (Fig. 7). Another possible explanation for this trend is that higher redshift galaxies need to be brighter to fulfil our flux density selection criteria, and these brighter galaxies tend to be warmer (e.g. Symeonidis et al. 2013; Kirkpatrick et al. 2017).

Any fitting methods with a range of temperatures and no explicit prior on the temperatures is effectively assigning a uniform prior to the temperatures. This is what our method does as do most photometric redshift fitting methods. In the low signal-to-noise regime the prior has a stronger influence on the posterior and so there will be a trend to fit mid-range temperatures rather than high or low temperatures. This naturally tempers the extremes of redshifts distributions based on the best redshift. However, the redshift PDFs are a reasonable representation of the information available.
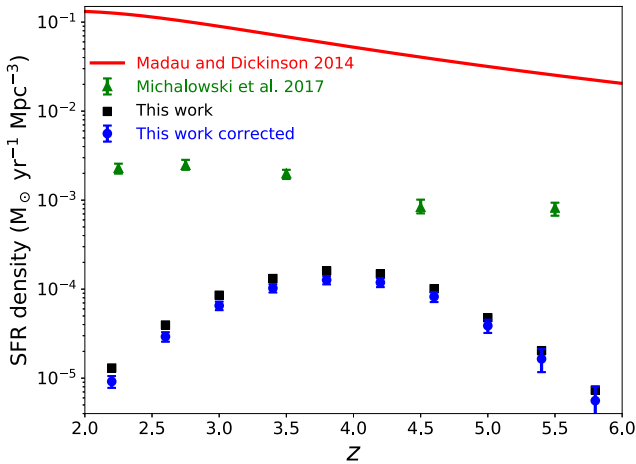
Figure 8. SFR density of sources with $S_{500} > 63$ mJy and $S_{500} > S_{350} > S_{250}$ in the HeLMS field in black squares, using the full redshift PDF. In blue is the corrected contribution of those sources, where contamination from AGN is removed and we corrected for flux boosting (see Sections 4.1 and 4.2). The red line is the Madau & Dickinson (2014) SFRD estimates for all sources in the Universe. The green triangles are the Michałowski et al. (2017) measurements of DSFGs with SFR > 300 M$_{\odot}$ yr^{-1} from two blank S2CLS fields. The maximum contribution to the total SFRD is 0.3 per cent at $z \simeq 4.2$.

4 RESULTS

4.1 Statistical properties

In Fig. 7, we show the SFR versus redshift distribution of our sources. Our sources have a median redshift of 3.6 ± 0.4 and a median SFR (uncorrected for flux boosting or the possible presence of gravitational lensing) of $5.2 \pm 1.9 \times 10^3$ M$_{\odot}$ yr^{-1}. All our galaxies could be classified as distant hyper-luminous infrared galaxies (HyLIRGS), i.e. with L_{IR} exceeding 10^{13} L$_{\odot}$ and a mean L_{IR} of 2.7×10^{13} L$_{\odot}$.

We find that 31.4 ± 4.7 per cent lie between redshifts of 4 and 6. This finding is consistent with Ivison et al. (2016), who found 33 ± 6 per cent of their sample to lie within this redshift range. The inferred space density (ρ_{obs}) in this redshift range is 1.1×10^{-8} Mpc^{-3}. Due to the predicted short lifetime for the starburst (t_{burst}) phase we need to apply a duty-cycle correction to the observed space density to infer the actual underlying space density (ρ) for these type of galaxies

$$\rho = t_{obs}/t_{burst} \times \rho_{obs}, \quad (4)$$

were t_{obs} is the time between $4 < z < 6$. For t_{burst} we assume 100 Myr, which is in agreement with their expected gas depletion times (Ivison et al. 2011; Bothwell et al. 2013). The final inferred space density estimate is thus 7×10^{-8} Mpc^{-3}. The assumption of 100 Myr is the same as used by Ivison et al. (2016) and while longer time-scales (0.5–1.0 Gyr) have been postulated (e.g. Lapi et al. 2014; Aversa et al. 2015) these would result in an even lower space density.

The primary difference between the Ivison et al. (2016) sample and our sample is that Ivison et al. (2016) used a $S_{500} > 30$ mJy selection where we use a $S_{500} > 63$ mJy sample. Therefore, our sample has a space density of about a factor of 10 lower than the Ivison et al. (2016) estimate of 6×10^{-7} Mpc^{-3}.

We use our sample to calculate the SFRD for bright 500 µm risers in the SPIRE bands as shown in Fig. 8. The contribution to the overall SFRD is below 1 per cent at any redshift. For comparison we

also show the SFRD results from the S2CLS $S_{850} \geq 4$ mJy selected sources, which is complete for galaxies with an SFR > 300 M$_{\odot}$ yr^{-1} (Michałowski et al. 2017). The Michałowski et al. (2017) result comes from 2 deg^2 blank fields, which observe the more common population of DSFGs and contribute more to the overall SFRD at any epoch.

4.1.1 Luminosity function

The SPIRE sources luminosity function and its evolution to $z \sim 4$ has been reported in Gruppioni et al. (2013). We can use this luminosity function as a basis to predict the number of galaxies we expect in our sample. To get an accurate estimate for our incompleteness we need to know the relative distribution of different galaxy types at these high luminosities and redshifts. The intrinsic colours of different galaxy types can be used to determine whether or not they fulfil our selection criteria as a function of redshift.

Due to the lack of information on the distribution of galaxy types at high redshift we have to extrapolate what we know about the distribution of SED shapes at lower redshift and luminosity to the redshifts and luminosities of our sample. We do this using the results from Symeonidis et al. (2013), who measured the correlation between average dust temperatures and infrared luminosities. They characterized the rising dust temperature with luminosity for a sample of $10^{11} < L_{IR}/L_{\odot} < 10^{12.7}$ galaxies, and, to provide a simple phenomenological characterization of this, we apply a linear fit in temperature versus $\log L_{IR}$ to predict the average temperature for $L_{IR}/L_{\odot} \geq 10^{12.5}$ galaxies. We also use the average value for the variance in the temperature for $L_{IR}/L_{\odot} > 10^{12}$ galaxies.

Using this temperature–luminosity–redshift distribution we draw 200 galaxies at every redshift between 1.5 and 8 ($\Delta z = 0.1$) and luminosities between $10^{12.5} < L_{IR} < 10^{15.0}$ ($\Delta \log L_{IR} = 0.1$) and then each galaxy is assigned a temperature drawn from a Gaussian with mean from the temperature–luminosity and a sigma of 6 K. This produces a mock catalogue of 325 000 galaxies, for which we have mock T, z, and L_{IR} values. We use the Casey (2012) MBB to calculate the expected flux densities at SPIRE and SCUBA-2 wavelengths for each galaxy. The upper limit of $L_{IR} = 10^{15.0}$ is used for practical reasons to simplify the drawing of a random luminosity. It was not intended to indicate a realistic physical limit. However, the number density is dropping off very steeply at high luminosity so exactly where this cut is made makes little difference to the outcome.

We add Gaussian noise with a mean of zero and a sigma of the mean instrumental error of our observations to simulate the variations caused by instrumental noise. On top of the Gaussian noise we also draw a correlated confusion noise estimate for every source using the COSMOS map (see Section 3.2), and we add this correlated confusion to our mock observed flux density estimates. Our novel way of adding the correlated confusion noise is crucial as it partly conserves the colour of the source. The standard deviation of the confusion noise we added is 6.7, 7.1, and 6.8 mJy at 250, 350, and 500 µm, respectively and together with the instrumental noise of order 7 mJy this leads to 1σ fluctuations of ~10 mJy. It will therefore not be uncommon that sources of order 30 mJy at 500 µm will be boosted to the selection criteria of 63 mJy due to the noise and the steepness of luminosity function.

We multiply the fraction of mock galaxies in every luminosity and redshift bin which fulfil our selection criteria by the expected space density for such galaxies (Gruppioni et al. 2013) to obtain the number of galaxies we would expect in the HeLMS field. This

Table 2. Red number counts from observations, from Béthermin et al. (2017), and from our mock catalogue based on Gruppioni et al. (2013) and Symeonidis et al. (2013). We created additional mock catalogues with different average temperatures to show the dependence on temperature for the predicted number counts. Error bars on the mock catalogue come from the error in the normalization of the Gruppioni et al. (2013) luminosity function, our observations error bars come from poison statistics. With the current large error bar sizes we can only exclude (difference $>3\sigma$) the T + 5 K model.

Model	Number count
Observed	200 ± 14
Béthermin et al. (2017)	172 ± 18
Symeonidis et al. (2013)	262^{+184}_{-103}
T + 5 K	54^{+38}_{-21}
T + 4 K	76^{+54}_{-30}
T + 3 K	85^{+61}_{-34}
T + 2 K	117^{+83}_{-46}
T + 1 K	170^{+121}_{-57}
T − 1 K	330^{+234}_{-130}
T − 2 K	373^{+264}_{-147}
T − 3 K	493^{+349}_{-194}
T − 4 K	611^{+433}_{-241}
T − 5 K	842^{+597}_{-332}

results in a total sample of $\sim260^{+180}_{-100}$ galaxies in our mock catalogue over an area of $274\,\mathrm{deg}^2$. This is mildly larger than, but consistent with, the 200 galaxies we observed in the HeLMS field. The error bars are based on the large error on the normalization of the luminosity function (Gruppioni et al. 2013). We do acknowledge that the consistency is partly due to the large error bars in this normalization.

We make an additional 10 mock catalogues where we modify the mean temperature in the relations of Symeonidis et al. (2013) to measure the effect of the average temperature of DSFGs on the observed number counts. In Table 2, we show the total number counts as function of (mean) temperature. It is clear that the number of observed galaxies is a strong function of temperature and it is therefore important to get a better understanding of the distribution

of galaxy types at high redshift to fully understand the number counts.

In Fig. 9, we show the resulting S_{500} and S_{850} number counts for our mock catalogues shown in Table 2. Our mock catalogue is consistent at S_{500} but overpredicts the number of bright sources at S_{850}, even when we raise the temperature of our mock catalogues with 5 K we keep overpredicting the number of sources at $S_{850} > 50$ mJy.

We use our mock model as input for EAZY to predict the observed luminosity function using our method. On top of the 200 galaxies we have already drawn at every redshift and luminosity bin we draw an additional 100 galaxies for every very bright bin ($L_{\mathrm{IR}}/L_\odot > 10^{13.5}$), an additional 300 galaxies for the $10^{13.1} < L_{\mathrm{IR}}/L_\odot < 10^{13.5}$ bins and an additional 500 galaxies for the $L_{\mathrm{IR}}/L_\odot < 10^{13.1}$ bins. these extra galaxies lead to a total mock size to test the luminosity function of 630 500 galaxies. These extra galaxies give us extra statistics on the lower end of the luminosity function, where galaxies are intrinsically not bright enough to be detected with our detection method but might be very occasionally scattered up by noise. In Fig. 10, we compare the predicted luminosity with the calculated luminosities for our galaxies.

From Fig. 10, we can see that the simulated galaxies are scattered up in luminosity due to confusion and instrumental noise. This is a flux boosting effect, well-known in sub-mm surveys (e.g. Coppin et al. 2005, 2006). From our mock catalogue we derive that 61 per cent of the mock galaxies which observational properties fulfil our selection criteria are intrinsically not bright enough and are scattered up due to confusion and instrumental noise. We use the average boosting factor (difference between input and output Luminosity of our Mock) to correct our SRFD in Fig. 8.

4.1.2 Comparison with simulations

The Simulated Infrared Dusty Extragalactic Sky (SIDES; Béthermin et al. 2017) includes a $274\,\mathrm{deg}^2$ simulation to match the size of the HeLMS field. The size of the model and its capability to simulate the observed FIR and submillimetre flux densities makes it ideal for comparison with our observations.

The main SIDES model predicts the FIR and submillimetre emission in a $2\,\mathrm{deg}^2$ light-cone, which simulates clustering by using abundance matching to populate dark matter haloes with galaxies according to their star formation evolution model. This model is
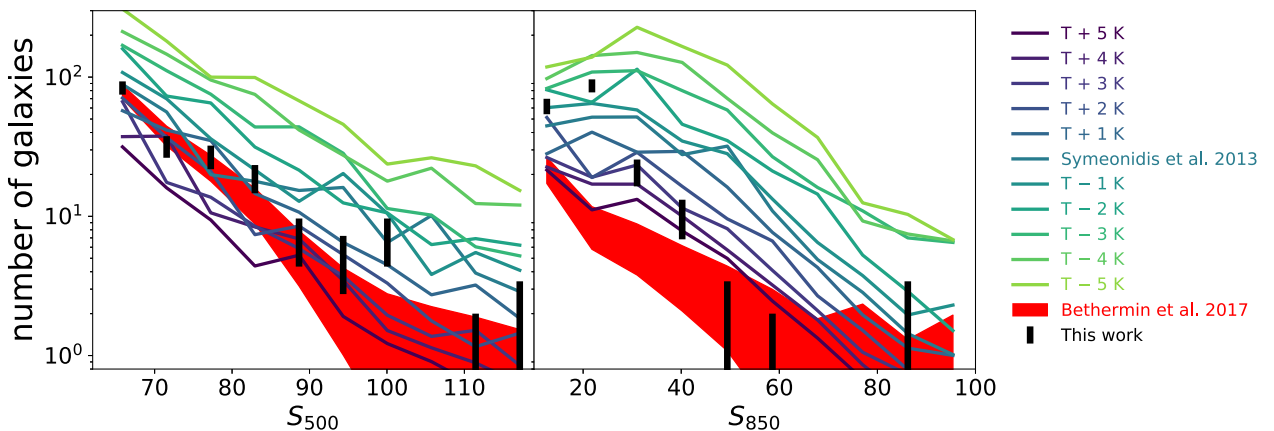
Figure 9. Number of galaxies which fulfil our selection criteria as function of 500 μm flux density on the left and as function of 850 μm on the right in black with Poisson error bars. In red, the number of galaxies from the SIDES model (Béthermin et al. 2017) in combination with observational errors. The coloured lines represent the number of galaxies we expect from the Gruppioni et al. (2013) luminosity function in combination with the nominal mean temperature, and variations on that mean temperature from Symeonidis et al. (2013).
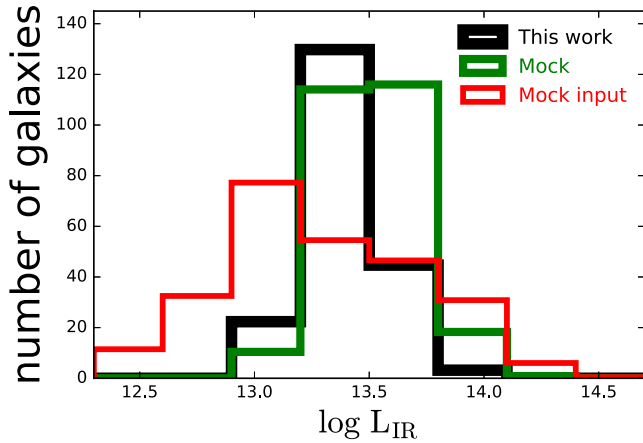
Figure 10. Luminosity histogram of 500 μm riser galaxies in the HeLMS field in black. In green, we show the output from our pipeline for the mock catalogue obtained from sampling galaxies from the Gruppioni et al. (2013) luminosity function and adding observational uncertainties to them. In red, we show the input luminosities for the mock sample shown in green.
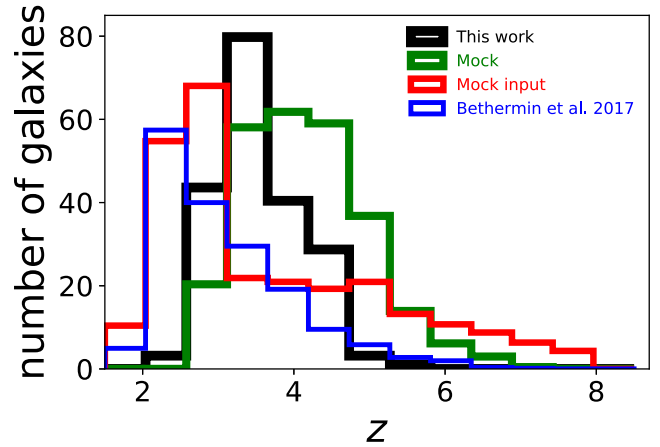

Figure 11. Redshift distributions of our observations (black), the mock (green) catalogue, the mock input (red), and the Béthermin et al. (2017) model (blue).

accurate in describing the number counts at 350 and 500 μm. This $2\,\mathrm{deg^2}$ light-cone is not a large enough volume to get accurate predictions for our rare sources. Béthermin et al. (2017) tackled this problem by producing the $274\,\mathrm{deg^2}$ simulation to predict number counts for much rarer (brighter) sources but this larger simulation does not contain any clustering estimates.

The number of sources in the $274\,\mathrm{deg^2}$ SIDES model which fulfil the Asboth et al. (2016) criteria is 22, and all are strongly lensed. This number goes down to 11 in the case we use our $S_{500} > 63$ mJy cut on top of the Asboth et al. (2016) criteria. These numbers are an order of magnitude lower that the bright red sources found in the HeLMS field.

Those results do not account for the effect of flux boosting by both instrumental and confusion noise. Béthermin et al. (2017) calculated this effect of flux boosting by adding random (Gaussian) instrumental and confusion noise to the fluxes. This increased the number count to 114 sources which fulfil the Asboth et al. (2016) criteria and 35 sources when we add $S_{500} > 63$ mJy constraint. The $2\,\mathrm{deg^2}$ SIDES model was used to calculate the effect of clustering on these number counts. They found that the confusion which arises from clustering increases the number of red sources by a factor of $1.7^{+1.9}_{-0.9}$. This leaves them with an estimate of 229^{+258}_{-121} sources which is within 1σ of the 477 sources found in Asboth et al. (2016). This boosting factor of $1.7^{+1.9}_{-0.9}$ is however not high enough to boost the 35 sources in the $274\,\mathrm{deg^2}$ SIDES model to the 200 sources found in the HeLMS field.

Our method of drawing correlated confusion noise estimates provides us with a different way of using the $274\,\mathrm{deg^2}$ SIDES model to predict the number of sources in the HeLMS field. We do this by adding both random Gaussian instrumental noise, and our correlated confusion noise estimates to the SIDES $274\,\mathrm{deg^2}$ catalogue. This noise increases the number of sources from 11 to 172 ± 18 (where the noise only accounts for different sets of random numbers and Poisson noise, and does not account for any other uncertainties in the SIDES model), which is very close to 200 sources which were detected with our selection criteria (see Table 2 and Fig. 9).

Seventeen per cent of these 172 sources are strongly lensed and the mean redshift is 3.1 ± 0.9. Fig. 11 shows the full redshift distribution of our data compared with the SIDES model and our mock catalogue.

From Fig. 11, we can see that the redshift distribution of the mock has a larger tail to higher redshifts than our observations. We test if there is any significant net bias we calculate the mean of the observed mock and input mock redshifts, we calculate the error on this mean using jack-knife samples. We find a different value for the mean redshift (4.17 ± 0.04 q.v. 3.69 ± 0.08), which is smaller than the rms of the refshifts of 0.6, but nevertheless statistically significant. Flux boosting can happen at every wavelength band but because of our 500 μm riser selection we are biased towards selecting galaxies which are boosted at 500 μm. These selected galaxies look therefore redder than they truly are, which results in a overestimate of the redshift. This argument mainly holds for galaxies which are intrinsically not red or bright enough to fulfil our selection criteria. For all galaxies we see the same trend as in Fig. 6, where our redshifts are overestimated at high redshift and under estimated at low redshifts. As we stated in more detail in Section 3.4 this trend is partly due to selection effects and due to the prior pushing us towards mean and not 'extreme' redshift estimates.

The $274\,\mathrm{deg^2}$ SIDES model has a comparable high-redshift tail, but this model peaks at lower redshift, causing the mean redshift to be lower (3.1 ± 0.07 q.v. 3.6 ± 0.04 from our observations).

4.2 SDSS and *WISE* quasars

We cross-matched the 188 galaxies with the SDSS quasar catalogue (Pâris et al. 2017) and found two matches within 20 arcsec. We test the change on a random alignment with an SDSS quasar by taking 50 000 random positions in the HeLMS field and see how many of these random positions match with an SDSS quasar within a 20 arcsec radius. The number of matches is 127, leading to a probability of 0.25 per cent that there is a random alignment within 20 arcsec. Using this statistics we would expect that there is a 38 per cent chance that at least one of our object is randomly aligned with an SDSS quasar and there is a probability of 8 per cent for at least two alignments.

HELMS_RED_80 is located 3 arcsec from SDSS_J005036.93+014449.1 which has a redshift of 3.4351 ± 0.0003. Our estimated photometric redshift is $3.63^{+0.68}_{-0.69}$, which is within 1σ agreement with the quasars spectroscopic redshift. The quasar is furthermore detected in *WISE*-1, *WISE*-2, and *WISE*-3. We use the intrinsic quasar SED derived in Symeonidis et al. (2016) in combination with the *WISE* magnitudes to calculate
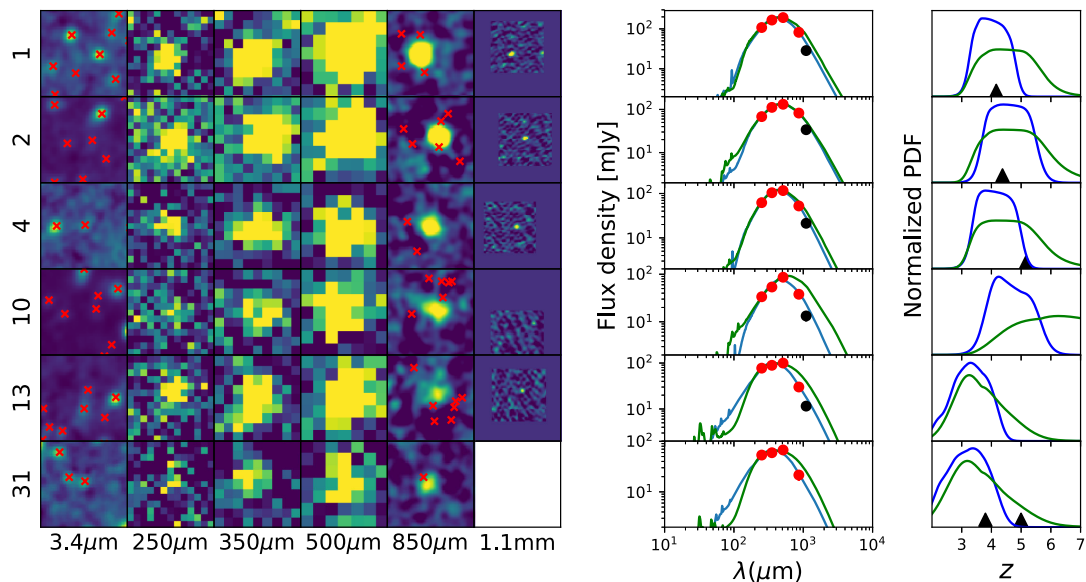
Figure 12. *WISE*-1 (3.4 μm), SPIRE (250, 350, 500 μm), SCUBA-2 (850 μm), and SMA (1.1 mm) 70 arcsec × 70 arcsec cut-outs of bright S_{850} sources in the HeLMS field with ancillary sub-mm interferometry data. The wavelength of each image is noted on the bottom of the plot in μm and the source ID (see Appendix A) on the left. The second on the right shows the best-fitting SED in blue, the best-fitting SED using only SPIRE in green, and the flux density from SPIRE and SCUBA-2 in red. The right-hand panel shows the redshift PDF of our sample in blue, and the PDF if we exclude the SCUBA-2 data in green (showing the improvement in constraining the redshift by including longer wavelength data). The black triangles show the spectroscopic redshifts derived from ALMA and CARMA, where the two black triangles for HELMS_RED_31 show the redshift in the case the line detection is the CO(5–4) or the CO(4–3) line. The red crosses on top of the *WISE* bands show 5σ source detections in *WISE*-1. On top of the SCUBA-2 image we overlay all SDSS-detected galaxies in red.

the AGN contribution to the FIR luminosity. This contribution is estimated at $\log(L_{\mathrm{FIR}}) = 12.97^{+0.11}_{-0.12}$ and is a factor of ∼3 lower that our measured luminosity. We thus conclude that it is likely that HELMS_RED_80 is associated with SDSS_J005036.93+014449.1 and that the quasar contaminates our SFR estimate.

HELMS_RED_421 is located 12 arcsec away from SDSS_J000127.11−010603.1 which has a redshift of 1.934 ± 0.001. Our estimated photometric redshift is $2.93^{+0.70}_{-0.79}$, which is in 1.3σ tension with the quasars spectroscopic redshift. The separation of 12 arcsec is furthermore in 2σ tension with our positions. The quasar is not detected in any *WISE* bands, but there is a nearby ($z = 0.163$) SDSS galaxy 9.0 arcsec away from our SPIRE detection which is detected in all four *WISE* bands >5σ (WISE_J000127.76−010607.5). Furthermore, WISE_J000126.74−010612.2 is located 9.6 arcsec away and is detected in *WISE*-1 and *WISE*-2 and WISE_J000127.44−010626.6 is located 12.4 arcsec away and has besides a *WISE*-1 and *WISE*-2 detection a 3.3σ detection in *WISE*-3. The location of our SPIRE source lies in the middles between those four *WISE*/SDSS sources, indicating that this source is likely contaminated by several of those galaxies. We tested the probabilistic de-blender XID+ (Hurley et al. 2017) using the default flat uniform flux prior (as used for the HELP data base, Vaccari 2016, Oliver et al., in preparation) to disentangle the SPIRE flux densities over the four sources. XID+ with a uniform flux prior, assigns the flux evenly among them as they are all located at roughly the same distance from the centre of the SPIRE emission. We note XID+ can be run with more sophisticated priors, using both SED and redshift information, however this requires thorough analysis and so we leave the nature of this SPIRE detection for future work.

HELMS_RED_421 may be associated with SDSS_J000127.11−010603.1 but would be consistent with a spurious coincidence. The percentage of the FIR luminosity

which is caused by the (potential) quasars is a function of the AGN luminosity (Rosario et al. 2012; Symeonidis et al. 2016; Symeonidis 2017), which we do not know. We therefore exclude the source from our final corrected SFRD.

4.3 Sub-mm interferometry

We use the high-resolution SMA data, the ALMA and the CARMA redshifts to more closely examine the properties of the subset of galaxies possessing this information. The images and SED fits of the six galaxies with interferometry data are shown in Fig. 12. We now discuss the sources individually below:

(i) HELMS_RED_1: The photometric redshift of $4.00^{+0.55}_{-0.52}$ is consistent with the spectroscopic redshift of 4.163 which is obtained with CO(4–3) and CO(5–4) line detections (Riechers et al., in preparation). The 500 μm flux density of 192 mJy suggests that the object is lensed (e.g. Negrello et al. 2017). This source was also detected with ACT with flux densities of $12.49 ± 1.74$, $35.11 ± 2.62$ and $72.32 ± 6.26$ mJy at 148 (2.0), 218 (1.4), and 278 (1.1) GHz (mm), respectively. Our best-fitting SED predicts flux densities of 7, 24, and 47 mJy at those frequencies, which are considerably lower. The SMA flux density at 1.1 mm is $28.6 ± 2.3$ mJy, which is less than half that of the ACT value at 278 GHz which is observed at a similar wavelength but with a much larger beam. The predicted 1.1 mm flux density from our best-fitting SED is 46.6 mJy. The nearest *WISE*-1 or SDSS source near to the SMA position is 15.6 arcsec away. The SMA position is 3.9 arcsec away from the SCUBA-2 position.

(ii) HELMS_RED_2: The photometric redshift of $4.59^{+0.67}_{-0.65}$ is consistent with the spectroscopic redshift of 4.373, which is obtained with CO(4–3) and CO(5–4) line detections (Riechers et al., in preparation). The 500 μm flux density of 132 mJy means the object

is likely to be lensed. The SMA flux density is 33.9 ± 2.25 and the predicted 1.1 mm flux density from our best-fitting SED is 53.9 mJy. The nearest *WISE*-1 or SDSS object near the SMA position is 2.0 arcsec away, the location of the source is J005258.53+061317.5 and has a *WISE*-1 AB magnitude of 17.5 ± 0.2. The SMA position is 2.0 arcsec away from the SCUBA-2 position.

(iii) HELMS_RED_4: The photometric redshift of $4.13^{+0.60}_{-0.57}$ is in 1.7σ tension with the spectroscopic redshift of 5.162, which is obtained with CO(5–4) and CO(6–5) line detections (Asboth et al. 2016). The 500 µm flux density of 116 mJy makes the object likely to be lensed. The SMA flux density is 21.3 ± 1.9 mJy and the predicted flux density at 1.1 mm from our best-fitting SED is 29.8 mJy. The nearest *WISE*-1 or SDSS object near the SMA position is 1.0 arcsec away, the location of the source is J002220.73−015520.2 and has a *WISE*-1 AB magnitude of 17.4 ± 0.2. The SMA position is 1.5 arcsec away from the SCUBA-2 position.

(iv) HELMS_RED_10: The photometric redshift is $4.62^{+0.75}_{-0.63}$. The SMA flux density of 13.3 ± 2.8 and the predicted 1.1 mm flux density from our best-fitting SED is 24.5 mJy. The nearest *WISE*-1 or SDSS object near the SMA position is 8.7 arcsec away. The SMA observations are not centred on the SCUBA-2 position and the brightest peak is 4.7σ. The SMA position is 13.4 arcsec away from the SCUBA-2 position. It is unclear if the SMA sources is the same source as our SPIRE/SCUBA-2 detection more detail of this sources will be provided in Greenslade et al. (in preparation).

(v) HELMS_RED_13: Our photometric redshift of $3.29^{+0.62}_{-0.64}$. The SMA flux density is 11.5 ± 1.8 mJy and the predicted flux density at 1.1 mm from our best-fitting SED is 19 mJy. The nearest *WISE*-1 or SDSS object near the SMA position is 3.6 arcsec away. The SMA position is 2.9 arcsec away from the SCUBA-2 position.

(vi) HELMS_RED_31: This object has a single line detection which might be either the CO(5–4) or the CO(4–3) transition (Asboth et al. 2016) suggesting a redshift of 3.798 or 4.997. The photometric redshift of $4.14^{+0.76}_{-0.73}$ is consistent with the lower redshift from and in a small (1.1σ) tension with $z = 4.997$. The nearest *WISE*-1 or SDSS source is 4 arcsec away from the SCUBA-2 position.

4.4 Extreme sources

We isolate a subset of potentially high-redshift extremely bright galaxies. This subset consists of galaxies which have a clear detection with SCUBA-2 ($S_{850} \geq 5\sigma$) as well as a redshift PDF which has 50 per cent of its probability at $z > 4$. In total, we find 21 galaxies fulfilling those conditions, which includes HELMS_RED_2, 4, 10, and 31. Fig. 13 shows the *WISE*-1, SPIRE, and SCUBA-2 cutouts of these sources, excluding the ones we already discussed in Section 4.3.

These sources might contain some of the highest redshift DSFGs ever detected. Therefore, this catalogue provides a high priority sample for spectroscopic follow-up with ALMA. High-resolution follow-up observations are also required for accurately determining the blending fraction (see Section 5.1) for these types of sources.

Our candidate with the highest chance of being a $z \geq 6$ galaxy is HELMS_RED_69. Its redshift is estimated to be $5.19^{+0.89}_{-0.92}$ and 19 per cent of its redshift PDF lies above a redshift of 6. Another remarkable feature of HELMS_RED_69 is that its 500 µm flux density is 1.5 times higher than that of HFLS3. There is a possibility that this source has been lensed by a foreground galaxy as we find an SDSS counterpart at a distance of 3.0 arcsec.

5 DISCUSSION

5.1 Blending and lensing

Due to the relatively large beam of the 500 µm data there is a high probability that in many cases some parts of the measured flux density comes from randomly aligned galaxies or companion galaxies of the main source (confusion; Nguyen et al. 2010).

ALMA observations (Hodge et al. 2013; Karim et al. 2013) of bright LABOCA ($S_{870} > 12$ mJy) sources in the 0.25 deg² LESS survey (Weiß et al. 2009) showed that these sources contain emission from several fainter sources with an upper limit of 9 mJy per source, in later work this fraction of sources breaking up is found to be less significant (Simpson et al. 2015). This indicates that there might be a maximum SFR for DSFGs of 10^3 M$_\odot$ yr^{-1} (Chabrier IMF). Bussmann et al. (2015) found that 20 out of 29 bright SPIRE sources ($S_{500} = 52$–134 mJy) break down into multiple ALMA sources, and of the nine isolated sources five have a magnification factor larger than 5. Simpson et al. (2015) found that 61^{+19}_{-15} per cent of their sample of bright galaxies (median $S_{850} \pm 0.4$ mJy) consist of a blend of two or more sources in the ALMA maps. Their sample was selected to be representative of the bright end of the 1 deg² deep 850 µm S2CLS field. The brightest detection with ALMA had a flux density of 12.9 ± 0.6 mJy and is considerably brighter than the sources observed in Karim et al. (2013). Michałowski et al. (2017) found that bright DSFGs found in SCUBA-2 blank fields (around 10 mJy) typically have a second component of about 1–2 mJy. Furthermore, they found that the bright end of the source counts is hardly affected by replacing from SCUBA-2 flux densities with those from ALMA. The survey was taken over an area of 2 deg².

The bright end of the Karim et al. (2013), Simpson et al. (2015), and Michałowski et al. (2017) sources are fainter than 20 mJy, and are thus much fainter than our Group 1 galaxies. Hence, it would be interesting to see if our brightest sources are also characterized by having a second component of about 1–2 mJy or a 61^{+19}_{-15} per cent blending fraction.

Prior-based source extraction (XID+ Hurley et al. 2017) to investigate multiplicities of bright *Herschel* sources at 250 µm in the COSMOS field show that the brightest component contributes roughly 40 per cent of the source flux density (Scudder et al. 2016).

The multiplicity due to blending seen in these studies is a potential concern. Blending of objects at the same redshift will not seriously impact on the redshift determination, although we will determine the luminosity and star formation of the combined system, rather than a single object. Blending of two (or more) objects at different redshifts will produce composite SEDs which are likely to elicit an intermediate redshift estimate. We derive from our mock observations that ∼60 per cent of our detected galaxies are likely to be scattered up to our selection criteria due to flux boosting partly caused by blending with foreground objects. Some of those boosting factors are as large as 0.5 dex, but can be explained by instrumental and confusion noise. An example of such a large effect might be HELMS_RED_421 where the SPIRE position is in the middle of three *WISE* sources and an SDSS detected quasar. Similar results were found in Donevski et al. (2017), where ∼40 per cent of selected 500 µm riser galaxies in a simulated map would intrinsically not have made their selection criteria of $S_{250} > 13.2$ mJy and $S_{500} > 30$ mJy.

The advantage with our sample is that we probed a much wider field, over 100 times wider than COSMOS and S2CLS and more than 1000 times bigger than the area targeted by the ALMA observations of the LESS field. Our sample is therefore expected to
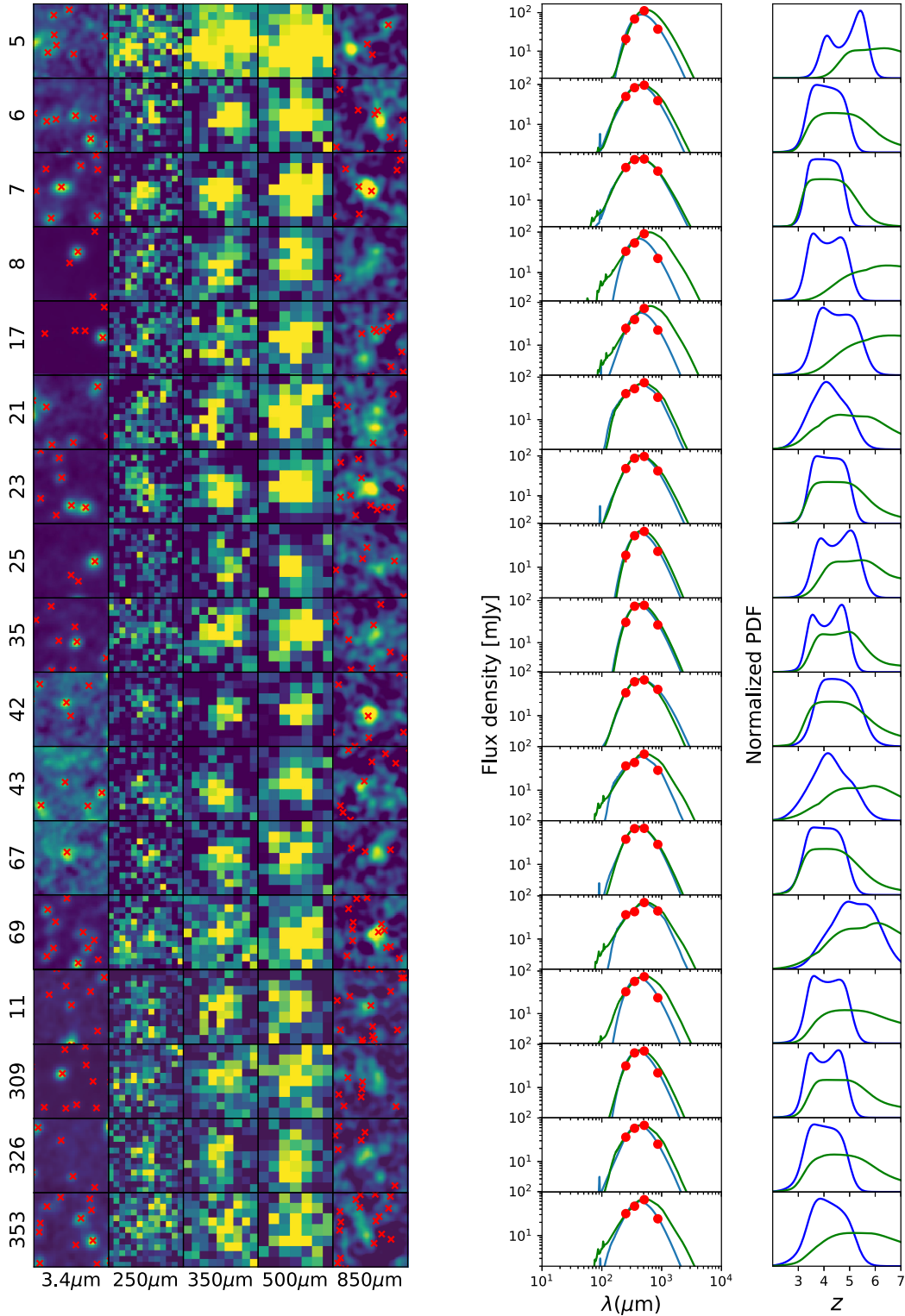
Figure 13. *WISE*-1 (3.4 μm), SPIRE (250, 350, 500 μm), and SCUBA-2 (850 μm) 70 arcsec × 70 arcsec cut-outs of bright S_{850} sources in the HeLMS field. The wavelength of each image is noted on the bottom of the plot in μm and the source ID (see Appendix A) on the left. The second on the right shows the best-fitting SED in blue, the best-fitting SED using only SPIRE in green, and the flux density from SPIRE and SCUBA-2 in red. The right-hand panel shows the redshift PDF of our sample in blue, and the PDF if we exclude the SCUBA-2 data in green (showing the improvement in constraining the redshift by including longer wavelength data). The red crosses on top of the *WISE* bands show 5σ source detections in *WISE*-1. We overlay all SDSS-detected galaxies in red over the SCUBA-2 images.
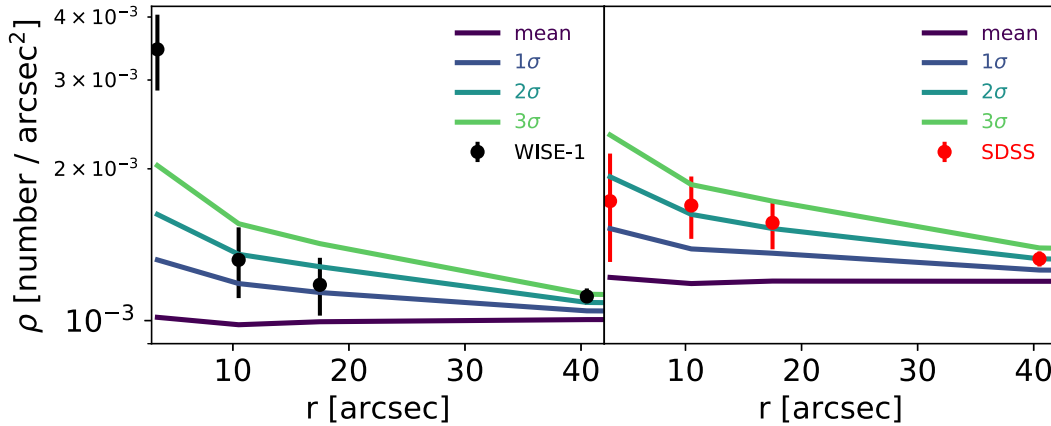
Figure 14. Surface density of *WISE*-1 sources (left, black) and SDSS galaxies (right, red). There is a significant increase in low-redshift sources (possible lenses) near our targets in comparison with average number counts (solid lines). The higher number density near our targets can be caused by an overlap of the redshift distribution of optical/NIR sources and sub-mm sources and/or a signature of foreground lensing.

be comprised of a much rarer and more luminous and less confused population of sources. However, a proper investigation of the blending of these objects is deferred until we are able to obtain high-resolution data of a significant sub-set.

HFLS3 has an observed flux density of 35.4 ± 0.9 mJy at 850 μm (Robson et al. 2014), which is comparable to our Group 1 galaxies. Riechers et al. (2013) found that HFLS3 is only marginally magnified by a factor of 1.2–1.5 by a foreground lens. This magnification factor was updated by Cooray et al. (2014) to a factor of 2.2 ± 0.3, which yields an SFR of 1320 $M_\odot$ yr^{-1}.

Another explanation for the high SFRs in our sample is that the galaxies might be lensed (Zavala et al. 2018). We do not expect to detect weak lensing from high-redshift lenses or even unambiguous confirmation of large magnifications from nearby lenses from our current data. We can however asses the likely incidence of lensing statistically by looking at the density of *WISE*-1 and SDSS sources near our SCUBA-2 detections. For this we use our Group 1 galaxies which have $>5\sigma$ SCUBA-2 detections. For this group we can use the SCUBA-2 positions with a statistical positional accuracy of $\sigma_{pos} = 0.6 \times \frac{FWHM}{S/N}$ (Ivison et al. 2007) which is of the order of 2 arcsec, which is comparable with the JCMT pointing accuracy of 2–3 arcsec. We combine these two uncertainties ($\sigma_u^2 = \sigma_{pos}^2 + \sigma_{JCMT}^2$) and assume that either the optical/NIR counterpart or the lens should lie within a $\approx 2\sigma_u \approx 7$ arcsec annulus around our source position.

We use this 7 arcsec aperture to count the number of 5σ *WISE*-1 detected objects near our Group 1 sources and find that 53 per cent have a nearby *WISE* galaxy. We calculate the significance of this number by using the same aperture at 64 (same number as Group 1 galaxies) random positions in the HeLMS field 1000 times. With these 1000 runs we can calculate both the expectation value and the 84.1, 97.8, and 99.9 percentiles.

In Fig. 14, we show our results for our 7 arcsec aperture and several larger apertures. It is clear that there is a significant overdensity of *WISE*-1 sources near our Group 1 galaxies. The total space density of *WISE*-1 sources is a factor of 3 higher, which is a strong indication that part of this sample is lensed (Wang et al. 2011). We perform the same measurement on a $S_{500} > 100$ mJy subset and find that seven of the nine sources have a *WISE*-1 counterpart within the 7 arcsec annulus. This leads to an even higher *WISE*-1 space density compared to our Group 1 sample, but due to the low number of galaxies this is less significant than our Group 1

overdensity. González-Nuevo et al. (2014) found a similar result by cross-correlating SDSS and GAMA $0.2 \leq z \leq 0.6$ galaxies with $S_{350} \geq 30$ mJy *H*-ATLAS sources. They found a $>10\sigma$ spatial correlation, which for non-overlapping redshift distributions can be explained by weak gravitation lensing, where the weak regime has a lensing factor smaller than 2.

We do, however, wish to stress that this is a statistical measurement, and we lack accurate enough positions and morphologies for our DSFGs to do a proper lensing analysis to yield a magnification estimate. Furthermore, we lack sufficiently deep optival data to find potential lenses at $z > 0.5$. For our estimates of the L_{IR} and SFR we do not take this significant foreground source detection into account.

An overlap between the redshift distribution of *WISE*-1 sources and 500 μm risers could provide another explanation for the excess *WISE*-1 sources seen near our high-redshift DSFGs. Ménard et al. (2013) used the cross-correlation between SDSS quasars and *WISE* sources to recover the redshift distribution of *WISE* sources. They found that there is a potential sub-sample of *WISE* sources with a redshifts >2, indicating that it is possible that our high-redshift sample could be detected in *WISE*. However, their red *WISE* sources with $z > 2$ are at least 1.2 magnitudes brighter in the *WISE*-2 band than in *WISE*-1 and several orders of magnitude brighter in the *WISE*-3 band.

We find that 34 of our 64 Group 1 galaxies have at least one *WISE*-1 source within the 7 arcsec aperture. Of these 33 closest *WISE* sources, only 2 have a *WISE*-2 magnitude 1.2 brighter than *WISE*-1. The remaining 31 are either undetected in *WISE*-2 (and we would have detected them if they were 1.2 magnitude brighter than in *WISE*-1) or they have a *WISE*-2 magnitude that is not bright enough to fall in the red sample. The non-red *WISE* sources have a mean redshift of 0.5 and are very unlikely to have a redshift above 1.5 Ménard et al. (2013).

High-resolution follow-up is required to properly assess the incidence of lensing and to resolve any blending issues and determine the merging, interacting or stable disc-like morphologies of the systems (e.g. Oteo et al. 2017a; Dye et al. 2018; Leung et al., in preparation). The high-resolution 870 μm ALMA continuum observations of 11 of our DSFGs show that 7 of them show disturbed morphologies, indicating strong lensing (Oteo et al. 2017b). These results show that lensing can explain some of the extremely high flux densities but also show that some galaxies are not strongly

lensed and do have extreme SFRs ($\gg 10^3$ M$_\odot$ yr^{-1}). For a full description of the ALMA data and the morphology of the sources, see Oteo et al. (2017b).

5.2 Space density

Ivison et al. (2016) compared their space density of DSFGs at $4 < z < 6$ to the space density of *UVJ* selected massive galaxies at $3.4 < z < 4.2$ (Straatman et al. 2014) which are predicted to form their stellar mass around redshift 5. Straatman et al. (2014) found a space density for massive $M_{stars} > 10^{11}$M$_\odot$ quiescent galaxies of 4×10^{-6} Mpc^{-3}, which is an order of magnitude higher than Ivison et al. (2016) and 2 orders of magnitude higher than our results of 7×10^{-8} Mpc^{-3}.

We can therefore make a similar conclusion to that of Ivison et al. (2016) for *H*-ATLAS ($S_{500} > 30$ mJy), i.e. that the HeLMS ($S_{500} > 63$ mJy) red sample cannot account for the massive quiescent galaxies found at $z \sim 3$–4. This can be confirmed by our measured SFRs (5000 M$_\odot$ yr^{-1}), which for a t_{burst} of 100 Myr generate a higher stellar mass of $M_{stars} \sim 5 \times 10^{11}M_\odot$ yr^{-1} than the (Straatman et al. 2014) sample. This suggests that part of our sample might go through a short phase ($\ll 100$ Myr) of extremely high star formation, or is lensed, or is more massive (and thus rarer) than the population probed by Straatman et al. (2014).

6 CONCLUSIONS

We have observed 188 high-redshift, dusty, star-forming galaxy candidates with the SCUBA-2 camera at the JCMT. The sample had been selected to be very red and bright at *Herschel* SPIRE wavelengths and was taken from the 274 deg^2 HerMES HeLMS field. We achieve a 1σ rms depth of $S_{850\,\mu m} = 4.3$ mJy and detected 87 per cent of our candidates with S/N > 3.

We developed a new method of incorporating correlated confusion noise into our SED fitting procedure.

We applied EAZY with a range of galaxy templates to determine the full redshift PDF. The addition of the longer wavelength 850 µm data improves our photometric redshifts which are systematically lower than with SPIRE data alone and reduces the estimated uncertainties from $\sigma_z/(1 + z) \approx 0.25$ to 0.19. Our photometric redshifts are consistent with the four spectroscopic redshifts available in our sample.

With this final PDF we compute the redshift, FIR luminosity, and SFRs of our sample. From these we computed the SFRD and showed that the population of 500 µm risers with $S_{500} > 63$ mJy contribute less than 1 per cent of the total SFRD at any epoch. The number density of 500 µm risers is consistent with a model extrapolated from the Gruppioni et al. (2013) FIR luminosity function and with the Béthermin et al. (2017) empirical model, contradicting previous tensions with physically motivated models. Consistency with the models arises from our novel way in adding both confusion and instrumental noise were ~ 60 per cent of the galaxies are predicted to be scattered up to our selection criteria due to flux boosting.

The excess number of *WISE*-1 sources near our DSFGs gives a strong indication that some of our sample may be lensed or that there is a surprising overlap with the redshift distribution of *WISE*-1 sources.

High-resolution SMA observations of five of our sources reveal that two of the sources have a *WISE*-1 source at the same position. In all cases the SMA flux density at 1.1 mm is lower than predicted from our best-fitting SED.

We identify a subset of 21 excellent very high-redshift DSFGs candidates, of which two are already identified as $z > 4$ DSFGs. This group is clearly detected by SCUBA-2 with a high probability that they lie above a redshift of 4. These 21 galaxies would be ideal targets for interferometric imaging and spectroscopy to get a better understanding of these high-redshift objects with extreme ($\gg 1000$ M$_\odot$ yr^{-1}) star formation.

Observing the high-redshift, dust-obscured Universe remains an important challenge for current day astronomy. Interferometry has the resolution and sensitivity to answer our questions about the SFR and nature of these obscured galaxies. With telescopes like ALMA it is still impractical to cover a large enough area of the sky to find a representative population of extreme star-forming sources. With our new catalogue we now possess an ideal target list for high-resolution and spectroscopic follow-up.

REFERENCES

Ahn C. P. et al., 2012, ApJS, 203, 21
Aretxaga I., Hughes D. H., Chapin E. L., Gaztañaga E., Dunlop J. S., Ivison R. J., 2003, MNRAS, 342, 759
Asboth V. et al., 2016, MNRAS, 462, 1989
Aversa R., Lapi A., de Zotti G., Shankar F., Danese L., 2015, ApJ, 810, 74
Baugh C. M., Lacey C. G., Frenk C. S., Granato G. L., Silva L., Bressan A., Benson A. J., Cole S., 2005, MNRAS, 356, 1191
Becker R. H., White R. L., Helfand D. J., 1995, ApJ, 450, 559
Berta S. et al., 2013, A&A, 551, A100
Béthermin M., Dole H., Lagache G., Le Borgne D., Penin A., 2011, A&A, 529, A4
Béthermin M. et al., 2012, ApJ, 757, L23
Béthermin M. et al., 2017, A&A, 607, A89
Bothwell M. S. et al., 2013, MNRAS, 429, 3047
Brammer G. B., van Dokkum P. G., Coppi P., 2008, ApJ, 686, 1503
Burgarella D. et al., 2013, A&A, 554, A70
Bussmann R. S. et al., 2015, ApJ, 812, 43
Carlstrom J. E. et al., 2011, PASP, 123, 568
Casey C. M., 2012, MNRAS, 425, 3094
Casey C. M. et al., 2012a, ApJ, 761, 139
Casey C. M. et al., 2012b, ApJ, 761, 140
Casey C. M., Narayanan D., Cooray A., 2014, Phys. Rep., 541, 45
Cesarsky C. J. et al., 1996, A&A, 315, L32
Chapin E. L. et al., 2011, MNRAS, 411, 505
Chapin E. L., Berry D. S., Gibb A. G., Jenness T., Scott D., Tilanus R. P. J., Economou F., Holland W. S., 2013, MNRAS, 430, 2545
Condon J. J., Cotton W. D., Greisen E. W., Yin Q. F., Perley R. A., Taylor G. B., Broderick J. J., 1998, AJ, 115, 1693
Conley A. et al., 2011, ApJ, 732, L35
Cooray A. et al., 2014, ApJ, 790, 40
Coppin K., Halpern M., Scott D., Borys C., Chapman S., 2005, MNRAS, 357, 1022
Coppin K. et al., 2006, MNRAS, 372, 1621
Coppin K. et al., 2008, MNRAS, 384, 1597
Cox P. et al., 2011, ApJ, 740, 63
Cutri R. M. et al., 2013, VizieR Online Data Catalog, 2328
Dempsey J. T. et al., 2013, MNRAS, 430, 2534
Donevski D. et al., 2017, A&A, preprint (arXiv:1709.00942)
Dowell C. D. et al., 2014, ApJ, 780, 75
Dye S. et al., 2018, MNRAS, 476, 4383
Eales S. et al., 2010, PASP, 122, 499
Fudamoto Y. et al., 2017, MNRAS, 472, 2028
Geach J. E. et al., 2017, MNRAS, 465, 1789
González-Nuevo J. et al., 2014, MNRAS, 442, 2680
Greve T. R. et al., 2012, ApJ, 756, 101
Griffin M. J. et al., 2010, A&A, 518, L3
Gruppioni C. et al., 2013, MNRAS, 432, 23
Haas M. et al., 2014, ApJ, 790, 46
Hayward C. C., Behroozi P. S., Somerville R. S., Primack J. R., Moreno J., Wechsler R. H., 2013, MNRAS, 434, 2572
Hodge J. A. et al., 2013, ApJ, 768, 91
Holland W. S. et al., 2013, MNRAS, 430, 2513
Holland W. S. et al., 2017, MNRAS, 470, 3606
Hurley P. D. et al., 2017, MNRAS, 464, 885
Ivison R. J. et al., 2007, MNRAS, 380, 199
Ivison R. J., Papadopoulos P. P., Smail I., Greve T. R., Thomson A. P., Xilouris E. M., Chapman S. C., 2011, MNRAS, 412, 1913
Ivison R. J. et al., 2016, ApJ, 832, 78
Karim A. et al., 2013, MNRAS, 432, 2
Kennicutt R. C., Jr, 1998, ARA&A, 36, 189
Kirkpatrick A. et al., 2017, ApJ, 843, 71
Klaas U., Haas M., Heinrichsen I., Schulz B., 1997, A&A, 325, L21
Lacey C. G., Baugh C. M., Frenk C. S., Benson A. J., Orsi A., Silva L., Granato G. L., Bressan A., 2010, MNRAS, 405, 2
Lapi A., Raimundo S., Aversa R., Cai Z.-Y., Negrello M., Celotti A., De Zotti G., Danese L., 2014, ApJ, 782, 69
Leung T. K. D., Riechers D. A., 2016, ApJ, 818, 196
Lonsdale C. J., Persson S. E., Matthews K., 1984, ApJ, 287, 95
Madau P., Dickinson M., 2014, ARA&A, 52, 415
Ménard B., Scranton R., Schmidt S., Morrison C., Jeong D., Budavari T., Rahman M., 2013, preprint (arXiv:1303.4722)
Michałowski M. J. et al., 2017, MNRAS, 469, 492
Narayanan D., Hayward C. C., Cox T. J., Hernquist L., Jonsson P., Younger J. D., Groves B., 2010, MNRAS, 401, 1613
Nayyeri H. et al., 2016, ApJ, 823, 17
Negrello M. et al., 2010, Science, 330, 800
Negrello M. et al., 2017, MNRAS, 465, 3558
Nguyen H. T. et al., 2010, A&A, 518, L5
Oliver S. J. et al., 2012, MNRAS, 424, 1614
Oteo I., Zwaan M. A., Ivison R. J., Smail I., Biggs A. D., 2017a, ApJ, 837, 182
Oteo I. et al., 2017b, ApJ, preprint (arXiv:1709.04191)
Pâris I. et al., 2017, A&A, 597, A79
Pilbratt G. L. et al., 2010, A&A, 518, L1
Polletta M. et al., 2007, ApJ, 663, 81
Riechers D. A. et al., 2013, Nature, 496, 329
Riechers D. A. et al., 2017, ApJ, 850, 1
Robson E. I. et al., 2014, ApJ, 793, 11
Rosario D. J. et al., 2012, A&A, 545, A45
Rowan-Robinson M. et al., 1997, MNRAS, 289, 490
Sayers J. et al., 2014, in Holland W. S., Zmuidzinas J., eds, Proc. SPIE Vol. 9153, Millimeter, Submillimeter, and Far-Infrared Detectors and Instrumentation for Astronomy VII. SPIE, Bellingham, p. 915304
Scoville N. et al., 2007, ApJS, 172, 1
Scudder J. M., Oliver S., Hurley P. D., Griffin M., Sargent M. T., Scott D., Wang L., Wardlow J. L., 2016, MNRAS, 460, 1119
Simpson J. M. et al., 2015, ApJ, 807, 128
Smail I., Ivison R. J., Blain A. W., 1997, ApJ, 490, L5
Smail I., Swinbank A. M., Ivison R. J., Ibar E., 2011, MNRAS, 414, L95
Soifer B. T. et al., 1984, ApJ, 283, L1
Straatman C. M. S. et al., 2014, ApJ, 783, L14
Strandet M. L. et al., 2016, ApJ, 822, 80
Strandet M. L. et al., 2017, ApJ, 842, L15
Su T. et al., 2017, MNRAS, 464, 968
Symeonidis M., 2017, MNRAS, 465, 1401
Symeonidis M. et al., 2013, MNRAS, 431, 2317
Symeonidis M., Giblin B. M., Page M. J., Pearson C., Bendo G., Seymour N., Oliver S. J., 2016, MNRAS, 459, 257
Vaccari M., 2016, Astrophysics and Space Science Proceedings, Vol. 42, The Universe of Digital Sky Surveys. Springer International Publishing, Switzerland, p. 71
Vieira J. D. et al., 2013, Nature, 495, 344
Wang L. et al., 2011, MNRAS, 414, 596
Wardlow J. L. et al., 2013, ApJ, 762, 59
Weiß A. et al., 2009, ApJ, 707, 1201
Weiß A. et al., 2013, ApJ, 767, 88
Wright E. L. et al., 2010, AJ, 140, 1868
York D. G. et al., 2000, AJ, 120, 1579
Zavala J. A. et al., 2018, Nat. Astron., 2, 56

APPENDIX A: TABLE OF SOURCE DETECTION

Table A1. Flux densities with instrumental errors, redshifts, and luminosities of our targets.

Source name	Name	S_{250} (mJy)	S_{350} (mJy)	S_{500} (mJy)	S_{850} (mJy)	phot-z	$\log(L_{\rm FIR}/{\rm L}_\odot)$
HerMES J004409.9+011823	HELMS_RED_1	108.1 ± 6.9	166.5 ± 6.0	191.8 ± 8.2	82.0 ± 3.9	$4.00^{+0.55}_{-0.52}$	$13.95^{+0.09}_{-0.09}$
HerMES J005258.9+061319	HELMS_RED_2	68.2 ± 6.0	111.6 ± 5.9	131.7 ± 6.9	82.4 ± 4.9	$4.59^{+0.67}_{-0.65}$	$13.92^{+0.09}_{-0.10}$
HerMES J003929.5+002424	HELMS_RED_3	140.8 ± 6.5	152.6 ± 6.3	162.1 ± 7.3	52.3 ± 4.5	$3.10^{+0.58}_{-0.65}$	$13.75^{+0.12}_{-0.17}$
HerMES J002220.8−015521	HELMS_RED_4	62.2 ± 6.1	104.0 ± 5.8	116.3 ± 6.6	52.4 ± 4.4	$4.13^{+0.60}_{-0.57}$	$13.76^{+0.09}_{-0.11}$
HerMES J005047.6+065720	HELMS_RED_5	20.8 ± 6.0	68.2 ± 6.4	112.0 ± 6.8	37.2 ± 4.2	$5.02^{+0.54}_{-0.91}$	$13.70^{+0.07}_{-0.13}$
HerMES J010053.9+030323	HELMS_RED_6	50.1 ± 6.8	83.3 ± 6.1	96.1 ± 7.8	39.3 ± 5.4	$4.10^{+0.63}_{-0.61}$	$13.65^{+0.10}_{-0.11}$
HerMES J003814.0+002250	HELMS_RED_7	73.3 ± 5.5	119.0 ± 6.0	122.9 ± 6.7	58.8 ± 3.6	$4.02^{+0.57}_{-0.57}$	$13.79^{+0.09}_{-0.10}$
HerMES J233802.0−011907	HELMS_RED_8	33.6 ± 6.5	53.8 ± 6.1	90.9 ± 7.6	22.4 ± 3.4	$4.13^{+0.67}_{-0.65}$	$13.46^{+0.10}_{-0.12}$
HerMES J002718.1+023946	HELMS_RED_9	65.2 ± 5.9	76.4 ± 5.7	99.3 ± 6.9	18.2 ± 3.6	$3.27^{+0.59}_{-0.56}$	$13.42^{+0.12}_{-0.13}$
HerMES J000304.4+024111	HELMS_RED_10	33.6 ± 5.7	53.9 ± 6.5	86.5 ± 6.9	37.9 ± 4.4	$4.62^{+0.75}_{-0.63}$	$13.63^{+0.10}_{-0.09}$
HerMES J004747.0+061444	HELMS_RED_11	71.4 ± 5.9	112.0 ± 6.0	114.6 ± 7.8	20.4 ± 6.0	$3.51^{+0.54}_{-0.60}$	$13.57^{+0.10}_{-0.13}$
HerMES J002115.6+013259	HELMS_RED_12	58.5 ± 6.3	80.5 ± 6.7	81.5 ± 7.3	36.7 ± 4.8	$3.67^{+0.64}_{-0.64}$	$13.57^{+0.11}_{-0.13}$
HerMES J002936.4+020706	HELMS_RED_13	77.4 ± 6.4	89.3 ± 6.1	100.0 ± 6.7	30.1 ± 5.0	$3.29^{+0.62}_{-0.64}$	$13.55^{+0.12}_{-0.16}$
HerMES J003847.0−021105	HELMS_RED_14	61.0 ± 5.9	75.1 ± 5.6	100.5 ± 7.0	19.7 ± 3.9	$3.42^{+0.59}_{-0.57}$	$13.45^{+0.11}_{-0.13}$
HerMES J011206.7+031417	HELMS_RED_15	54.4 ± 5.8	78.7 ± 5.9	92.2 ± 7.4	17.8 ± 6.3	$3.60^{+0.61}_{-0.59}$	$13.48^{+0.11}_{-0.13}$
HerMES J002959.4+032138	HELMS_RED_16	47.5 ± 5.8	78.7 ± 6.3	100.0 ± 6.5	26.9 ± 5.7	$3.98^{+0.62}_{-0.61}$	$13.57^{+0.09}_{-0.12}$
HerMES J005352.1+023916	HELMS_RED_17	24.6 ± 6.6	39.7 ± 6.4	72.0 ± 6.7	22.5 ± 3.6	$4.47^{+0.78}_{-0.72}$	$13.46^{+0.11}_{-0.12}$
HerMES J000727.1+015626	HELMS_RED_19	53.9 ± 6.1	72.5 ± 6.4	81.6 ± 7.0	40.9 ± 3.4	$3.90^{+0.67}_{-0.65}$	$13.60^{+0.10}_{-0.13}$
HerMES J003909.3+020247	HELMS_RED_21	41.0 ± 5.9	53.5 ± 6.1	74.3 ± 7.5	33.6 ± 4.6	$4.17^{+0.74}_{-0.71}$	$13.55^{+0.11}_{-0.13}$
HerMES J235411.8−082912	HELMS_RED_22	40.9 ± 6.5	57.8 ± 6.2	71.3 ± 6.8	20.6 ± 5.4	$3.80^{+0.69}_{-0.66}$	$13.43^{+0.11}_{-0.13}$
HerMES J004532.6+000121	HELMS_RED_23	48.2 ± 6.7	87.6 ± 6.3	97.2 ± 7.4	42.1 ± 4.9	$4.20^{+0.63}_{-0.61}$	$13.67^{+0.10}_{-0.11}$
HerMES J234805.1−052135	HELMS_RED_25	18.7 ± 5.6	52.0 ± 6.3	65.2 ± 7.3	22.9 ± 3.5	$4.56^{+0.68}_{-0.78}$	$13.46^{+0.09}_{-0.12}$
HerMES J003750.7+003323	HELMS_RED_28	66.4 ± 5.6	85.3 ± 5.9	92.9 ± 6.6	16.2 ± 4.2	$3.25^{+0.55}_{-0.56}$	$13.42^{+0.11}_{-0.13}$
HerMES J232404.6−055123	HELMS_RED_30	51.0 ± 5.9	76.8 ± 6.5	79.1 ± 7.4	33.5 ± 4.3	$3.82^{+0.64}_{-0.61}$	$13.55^{+0.11}_{-0.12}$
HerMES J002737.4−020801	HELMS_RED_31	42.0 ± 6.9	49.4 ± 6.0	75.3 ± 6.9	31.9 ± 3.9	$4.14^{+0.76}_{-0.73}$	$13.53^{+0.11}_{-0.14}$
HerMES J232133.3−040621	HELMS_RED_32	34.3 ± 5.6	63.5 ± 6.3	77.7 ± 7.0	14.4 ± 4.8	$3.89^{+0.61}_{-0.69}$	$13.40^{+0.10}_{-0.14}$
HerMES J004118.5+015537	HELMS_RED_33	34.7 ± 6.0	39.9 ± 6.1	64.4 ± 7.0	17.6 ± 3.5	$3.75^{+0.76}_{-0.76}$	$13.32^{+0.12}_{-0.16}$
HerMES J004302.6+011416	HELMS_RED_35	30.7 ± 6.6	73.7 ± 6.0	77.4 ± 7.3	26.5 ± 3.5	$4.23^{+0.59}_{-0.71}$	$13.52^{+0.08}_{-0.13}$
HerMES J001848.5−061051	HELMS_RED_36	46.6 ± 5.6	61.0 ± 6.2	66.0 ± 6.9	17.4 ± 4.5	$3.43^{+0.66}_{-0.64}$	$13.35^{+0.12}_{-0.15}$
HerMES J005254.9+032931	HELMS_RED_37	55.4 ± 6.0	90.0 ± 6.0	91.3 ± 7.4	30.6 ± 4.5	$3.79^{+0.59}_{-0.58}$	$13.57^{+0.10}_{-0.12}$
HerMES J000400.8−043103	HELMS_RED_38	53.4 ± 5.3	59.5 ± 5.7	67.4 ± 6.9	21.6 ± 4.6	$3.20^{+0.69}_{-0.74}$	$13.36^{+0.14}_{-0.19}$
HerMES J002822.0−021634	HELMS_RED_39	39.8 ± 6.0	54.7 ± 6.1	64.9 ± 6.9	16.2 ± 4.6	$3.61^{+0.68}_{-0.65}$	$13.34^{+0.12}_{-0.14}$
HerMES J234431.9−061852	HELMS_RED_40	59.5 ± 5.6	89.5 ± 5.8	92.2 ± 7.3	39.8 ± 4.5	$3.83^{+0.60}_{-0.59}$	$13.63^{+0.10}_{-0.12}$
HerMES J234647.8+000525	HELMS_RED_41	74.6 ± 5.8	95.4 ± 5.8	100.5 ± 7.0	23.6 ± 3.4	$3.30^{+0.55}_{-0.54}$	$13.50^{+0.11}_{-0.13}$
HerMES J002741.3−011650	HELMS_RED_42	33.1 ± 5.4	59.0 ± 5.7	64.9 ± 6.5	39.5 ± 3.8	$4.53^{+0.75}_{-0.71}$	$13.60^{+0.10}_{-0.12}$
HerMES J004656.1+013751	HELMS_RED_43	36.1 ± 5.8	43.4 ± 5.9	67.6 ± 6.8	28.7 ± 5.3	$4.24^{+0.82}_{-0.76}$	$13.50^{+0.11}_{-0.13}$
HerMES J004237.7+020457	HELMS_RED_45	49.3 ± 6.2	66.1 ± 6.0	87.6 ± 7.3	17.3 ± 5.1	$3.60^{+0.63}_{-0.60}$	$13.43^{+0.11}_{-0.13}$
HerMES J233247.6+003632	HELMS_RED_46	46.3 ± 5.9	72.9 ± 6.0	75.8 ± 6.8	29.4 ± 3.4	$3.84^{+0.63}_{-0.60}$	$13.52^{+0.10}_{-0.12}$
HerMES J003531.5+001536	HELMS_RED_49	52.2 ± 6.3	75.1 ± 5.7	81.7 ± 6.7	26.9 ± 3.8	$3.69^{+0.62}_{-0.60}$	$13.51^{+0.10}_{-0.12}$
HerMES J002937.6+002617	HELMS_RED_50	50.3 ± 6.1	66.8 ± 6.2	67.5 ± 7.1	16.1 ± 3.6	$3.31^{+0.63}_{-0.61}$	$13.33^{+0.13}_{-0.14}$
HerMES J232908.1−050653	HELMS_RED_51	44.3 ± 6.4	69.1 ± 6.1	76.8 ± 7.0	23.2 ± 4.5	$3.80^{+0.63}_{-0.62}$	$13.47^{+0.11}_{-0.12}$
HerMES J232342.0−035109	HELMS_RED_53	34.3 ± 5.6	36.3 ± 6.2	65.9 ± 7.6	19.1 ± 5.0	$3.87^{+0.80}_{-0.83}$	$13.36^{+0.13}_{-0.16}$
HerMES J234522.9+015601	HELMS_RED_54	46.2 ± 6.4	75.1 ± 5.9	79.6 ± 6.9	19.4 ± 3.6	$3.64^{+0.59}_{-0.61}$	$13.43^{+0.10}_{-0.13}$
HerMES J004600.3+065559	HELMS_RED_56	70.6 ± 6.0	85.6 ± 6.9	98.1 ± 7.6	17.9 ± 4.5	$3.23^{+0.57}_{-0.56}$	$13.44^{+0.11}_{-0.15}$
HerMES J001029.7−025524	HELMS_RED_57	32.5 ± 5.6	56.3 ± 5.9	70.6 ± 7.2	15.1 ± 3.3	$3.80^{+0.62}_{-0.59}$	$13.34^{+0.10}_{-0.13}$
HerMES J233943.0−013939	HELMS_RED_58	51.0 ± 6.2	66.8 ± 6.2	81.2 ± 7.1	19.2 ± 3.6	$3.50^{+0.62}_{-0.59}$	$13.41^{+0.11}_{-0.13}$

Table A1 – *continued*

Source name	Name	S_{250} (mJy)	S_{350} (mJy)	S_{500} (mJy)	S_{850} (mJy)	phot-z	$\log(L_{\mathrm{FIR}}/\mathrm{L}_\odot)$
HerMES J232849.6+010843	HELMS_RED_60	56.0 ± 5.7	95.3 ± 5.7	99.2 ± 6.9	35.3 ± 4.5	$3.92^{+0.58}_{-0.58}$	$13.62^{+0.10}_{-0.11}$
HerMES J001432.9+014530	HELMS_RED_61	60.7 ± 5.9	75.1 ± 5.8	81.5 ± 6.9	27.7 ± 3.4	$3.42^{+0.63}_{-0.63}$	$13.49^{+0.12}_{-0.14}$
HerMES J002319.1+001557	HELMS_RED_62	47.7 ± 5.9	60.9 ± 6.1	78.4 ± 7.3	20.9 ± 3.6	$3.58^{+0.66}_{-0.62}$	$13.42^{+0.11}_{-0.14}$
HerMES J233755.3−053318	HELMS_RED_64	48.4 ± 6.1	61.2 ± 6.5	66.1 ± 7.5	22.0 ± 6.0	$3.45^{+0.70}_{-0.72}$	$13.40^{+0.13}_{-0.16}$
HerMES J000947.0+034432	HELMS_RED_65	39.4 ± 5.6	57.1 ± 5.9	77.4 ± 6.8	22.9 ± 3.3	$3.88^{+0.66}_{-0.60}$	$13.45^{+0.10}_{-0.13}$
HerMES J235922.9−043705	HELMS_RED_67	37.8 ± 6.4	66.0 ± 6.0	67.0 ± 7.8	28.7 ± 4.1	$4.01^{+0.67}_{-0.65}$	$13.49^{+0.11}_{-0.12}$
HerMES J235808.7+005553	HELMS_RED_68	55.4 ± 5.6	73.9 ± 6.1	76.1 ± 6.5	32.7 ± 3.8	$3.60^{+0.63}_{-0.64}$	$13.52^{+0.11}_{-0.14}$
HerMES J000900.6+050709	HELMS_RED_69	36.6 ± 6.2	43.1 ± 6.0	70.2 ± 6.9	44.7 ± 4.8	$5.19^{+0.89}_{-0.92}$	$13.70^{+0.10}_{-0.13}$
HerMES J004019.0+052714	HELMS_RED_71	28.2 ± 5.6	49.8 ± 6.1	63.8 ± 7.1	10.0 ± 3.6	$3.71^{+0.65}_{-0.68}$	$13.25^{+0.11}_{-0.15}$
HerMES J005227.0+020027	HELMS_RED_72	66.9 ± 6.1	71.6 ± 6.2	84.1 ± 7.1	15.7 ± 4.6	$3.04^{+0.66}_{-0.67}$	$13.36^{+0.14}_{-0.19}$
HerMES J001813.6+053159	HELMS_RED_76	70.7 ± 6.0	75.6 ± 6.0	85.6 ± 6.2	17.5 ± 3.7	$3.02^{+0.63}_{-0.64}$	$13.38^{+0.14}_{-0.16}$
HerMES J000056.0+010231	HELMS_RED_77	70.4 ± 6.4	71.2 ± 6.1	84.4 ± 8.3	17.4 ± 4.9	$2.89^{+0.70}_{-0.80}$	$13.35^{+0.15}_{-0.24}$
HerMES J002552.3+031329	HELMS_RED_79	46.6 ± 6.0	65.7 ± 6.1	73.6 ± 6.8	12.0 ± 3.5	$3.32^{+0.60}_{-0.60}$	$13.30^{+0.12}_{-0.14}$
HerMES J005037.1+014449	HELMS_RED_80	44.2 ± 5.7	59.8 ± 6.1	64.5 ± 7.8	25.1 ± 3.7	$3.63^{+0.68}_{-0.69}$	$13.43^{+0.11}_{-0.15}$
HerMES J004724.4+010119	HELMS_RED_82	47.4 ± 6.9	75.8 ± 6.0	76.2 ± 7.6	36.2 ± 5.0	$3.96^{+0.67}_{-0.65}$	$13.57^{+0.11}_{-0.13}$
HerMES J235020.1−065224	HELMS_RED_84	67.5 ± 6.1	82.4 ± 6.5	84.0 ± 7.3	10.3 ± 4.7	$3.02^{+0.57}_{-0.57}$	$13.34^{+0.13}_{-0.15}$
HerMES J233823.1−042924	HELMS_RED_86	48.9 ± 6.5	58.1 ± 6.1	63.2 ± 7.5	22.5 ± 5.8	$3.37^{+0.73}_{-0.78}$	$13.38^{+0.14}_{-0.18}$
HerMES J002058.4+002114	HELMS_RED_88	36.3 ± 5.9	54.2 ± 6.0	63.8 ± 6.8	24.8 ± 3.5	$3.95^{+0.70}_{-0.66}$	$13.44^{+0.11}_{-0.13}$
HerMES J234940.0−025551	HELMS_RED_89	46.0 ± 6.3	58.5 ± 6.5	85.2 ± 6.5	7.4 ± 5.0	$3.37^{+0.65}_{-0.63}$	$13.32^{+0.12}_{-0.14}$
HerMES J010040.6+051550	HELMS_RED_95	52.0 ± 6.4	62.6 ± 6.1	78.9 ± 7.6	18.3 ± 3.8	$3.40^{+0.65}_{-0.62}$	$13.38^{+0.12}_{-0.15}$
HerMES J001533.3−054652	HELMS_RED_96	37.8 ± 6.3	51.6 ± 6.0	63.9 ± 7.1	19.1 ± 3.8	$3.72^{+0.71}_{-0.68}$	$13.36^{+0.13}_{-0.14}$
HerMES J232014.8−045552	HELMS_RED_98	20.4 ± 6.5	34.4 ± 6.0	74.2 ± 7.4	17.8 ± 4.9	$4.58^{+0.82}_{-0.79}$	$13.41^{+0.11}_{-0.13}$
HerMES J235221.4−043114	HELMS_RED_101	33.7 ± 5.7	58.3 ± 5.4	63.7 ± 7.3	17.8 ± 4.4	$3.87^{+0.65}_{-0.66}$	$13.37^{+0.11}_{-0.13}$
HerMES J004526.1+031638	HELMS_RED_104	48.6 ± 5.8	69.4 ± 5.6	76.6 ± 6.9	29.9 ± 4.3	$3.78^{+0.64}_{-0.63}$	$13.52^{+0.10}_{-0.13}$
HerMES J005134.1+053502	HELMS_RED_105	51.9 ± 5.9	61.2 ± 6.3	73.4 ± 7.6	24.8 ± 5.4	$3.46^{+0.68}_{-0.73}$	$13.43^{+0.13}_{-0.16}$
HerMES J232033.8−020958	HELMS_RED_106	56.9 ± 6.3	72.9 ± 6.5	74.8 ± 7.3	23.7 ± 6.4	$3.41^{+0.66}_{-0.67}$	$13.45^{+0.12}_{-0.15}$
HerMES J233052.3−060958	HELMS_RED_107	52.0 ± 6.3	59.6 ± 6.2	80.1 ± 7.3	21.9 ± 4.7	$3.48^{+0.68}_{-0.71}$	$13.42^{+0.12}_{-0.17}$
HerMES J233554.3−054408	HELMS_RED_108	46.6 ± 6.0	72.3 ± 6.6	86.1 ± 7.5	16.6 ± 4.2	$3.61^{+0.59}_{-0.62}$	$13.42^{+0.11}_{-0.13}$
HerMES J000208.8−015521	HELMS_RED_110	42.9 ± 5.7	57.3 ± 6.3	71.8 ± 6.8	20.9 ± 4.7	$3.72^{+0.64}_{-0.64}$	$13.42^{+0.12}_{-0.12}$
HerMES J235003.0−015825	HELMS_RED_114	41.9 ± 6.2	65.6 ± 6.0	77.8 ± 6.7	23.3 ± 4.9	$3.89^{+0.65}_{-0.62}$	$13.48^{+0.10}_{-0.13}$
HerMES J010631.8+015002	HELMS_RED_117	42.9 ± 6.4	46.8 ± 5.7	63.4 ± 7.4	19.0 ± 4.0	$3.42^{+0.77}_{-0.83}$	$13.32^{+0.15}_{-0.19}$
HerMES J003943.5+003955	HELMS_RED_118	32.7 ± 6.1	57.0 ± 6.1	73.7 ± 7.0	23.5 ± 3.9	$4.13^{+0.67}_{-0.65}$	$13.46^{+0.10}_{-0.12}$
HerMES J233208.3−022211	HELMS_RED_119	34.7 ± 6.0	57.5 ± 6.0	75.4 ± 7.0	25.7 ± 6.4	$4.20^{+0.71}_{-0.66}$	$13.51^{+0.10}_{-0.12}$
HerMES J005708.2+023637	HELMS_RED_123	35.1 ± 5.9	55.3 ± 5.8	79.7 ± 6.8	9.7 ± 4.7	$3.68^{+0.66}_{-0.67}$	$13.33^{+0.11}_{-0.15}$
HerMES J000000.7−054310	HELMS_RED_124	51.8 ± 6.6	62.2 ± 6.2	66.9 ± 6.4	21.8 ± 4.3	$3.35^{+0.69}_{-0.73}$	$13.39^{+0.13}_{-0.18}$
HerMES J233521.4−040227	HELMS_RED_126	39.6 ± 6.2	44.6 ± 6.9	63.9 ± 7.7	21.7 ± 4.6	$3.69^{+0.76}_{-0.81}$	$13.37^{+0.13}_{-0.17}$
HerMES J010433.0+044510	HELMS_RED_127	51.7 ± 6.1	62.1 ± 7.0	75.0 ± 8.7	19.7 ± 4.5	$3.38^{+0.68}_{-0.69}$	$13.38^{+0.12}_{-0.17}$
HerMES J235712.0−041341	HELMS_RED_134	53.6 ± 5.8	60.8 ± 5.5	70.4 ± 8.0	20.6 ± 4.0	$3.21^{+0.70}_{-0.76}$	$13.36^{+0.14}_{-0.19}$
HerMES J235833.6−042150	HELMS_RED_135	62.4 ± 6.2	71.8 ± 6.0	81.8 ± 7.3	12.3 ± 4.1	$3.06^{+0.61}_{-0.59}$	$13.32^{+0.13}_{-0.16}$
HerMES J004700.2+004214	HELMS_RED_136	46.6 ± 5.5	63.3 ± 6.0	63.8 ± 7.5	18.5 ± 3.7	$3.43^{+0.64}_{-0.64}$	$13.35^{+0.11}_{-0.15}$
HerMES J004434.7+070159	HELMS_RED_137	35.2 ± 6.2	42.3 ± 6.2	66.0 ± 7.5	17.3 ± 4.1	$3.75^{+0.76}_{-0.81}$	$13.33^{+0.12}_{-0.16}$
HerMES J011130.9+041443	HELMS_RED_139	44.2 ± 6.8	63.4 ± 6.2	64.2 ± 7.9	23.6 ± 4.6	$3.63^{+0.70}_{-0.69}$	$13.42^{+0.12}_{-0.15}$
HerMES J003651.3−015617	HELMS_RED_140	29.8 ± 6.3	51.8 ± 5.7	65.4 ± 7.6	13.5 ± 4.0	$3.84^{+0.66}_{-0.70}$	$13.31^{+0.11}_{-0.14}$
HerMES J233832.1−040953	HELMS_RED_142	27.3 ± 6.2	42.4 ± 6.1	66.7 ± 7.7	22.9 ± 4.7	$4.35^{+0.79}_{-0.72}$	$13.44^{+0.11}_{-0.12}$
HerMES J000407.6−050014	HELMS_RED_143	33.5 ± 6.6	49.4 ± 6.3	73.8 ± 7.4	15.1 ± 4.4	$3.86^{+0.70}_{-0.67}$	$13.36^{+0.11}_{-0.13}$
HerMES J005213.2+000447	HELMS_RED_146	54.3 ± 5.6	80.6 ± 6.2	81.3 ± 7.8	19.2 ± 5.4	$3.52^{+0.59}_{-0.59}$	$13.44^{+0.11}_{-0.12}$
HerMES J003512.0+010758	HELMS_RED_153	59.0 ± 6.0	72.6 ± 6.2	91.4 ± 7.1	12.5 ± 5.4	$3.32^{+0.60}_{-0.59}$	$13.40^{+0.12}_{-0.13}$
HerMES J235157.2−044058	HELMS_RED_154	29.4 ± 5.7	40.2 ± 6.7	63.4 ± 6.8	20.2 ± 4.4	$4.12^{+0.78}_{-0.70}$	$13.40^{+0.12}_{-0.13}$
HerMES J235752.2−040711	HELMS_RED_155	25.4 ± 5.6	40.3 ± 5.9	68.3 ± 6.7	20.1 ± 4.5	$4.38^{+0.77}_{-0.70}$	$13.42^{+0.10}_{-0.12}$
HerMES J233623.2+000108	HELMS_RED_160	54.7 ± 6.2	58.9 ± 6.4	69.2 ± 7.5	10.8 ± 3.5	$2.93^{+0.67}_{-0.73}$	$13.21^{+0.14}_{-0.22}$

Table A1 – *continued*

Source name	Name	S_{250} (mJy)	S_{350} (mJy)	S_{500} (mJy)	S_{850} (mJy)	phot-z	$\log(L_{FIR}/L_\odot)$
HerMES J232847.2−053724	HELMS_RED_161	46.6 ± 6.5	65.7 ± 5.6	67.4 ± 8.0	33.1 ± 4.5	$3.80^{+0.71}_{-0.69}$	$13.51^{+0.11}_{-0.14}$
HerMES J010906.7+052709	HELMS_RED_163	39.2 ± 6.4	51.9 ± 6.0	63.5 ± 8.3	18.6 ± 5.0	$3.63^{+0.74}_{-0.73}$	$13.36^{+0.12}_{-0.16}$
HerMES J004909.5+005712	HELMS_RED_165	25.6 ± 5.9	43.9 ± 5.5	63.1 ± 6.8	11.7 ± 3.9	$3.91^{+0.71}_{-0.71}$	$13.28^{+0.11}_{-0.14}$
HerMES J235924.0−075406	HELMS_RED_169	30.5 ± 6.8	54.6 ± 6.3	65.0 ± 7.3	17.2 ± 4.0	$3.92^{+0.68}_{-0.69}$	$13.37^{+0.11}_{-0.13}$
HerMES J004623.3+000425	HELMS_RED_173	27.4 ± 5.8	31.1 ± 5.9	64.7 ± 7.1	16.2 ± 3.6	$4.05^{+0.84}_{-0.78}$	$13.31^{+0.13}_{-0.15}$
HerMES J000326.9−041214	HELMS_RED_174	19.4 ± 5.9	56.1 ± 6.3	68.4 ± 7.5	12.8 ± 4.5	$4.20^{+0.63}_{-0.81}$	$13.37^{+0.10}_{-0.15}$
HerMES J233254.6+001616	HELMS_RED_179	62.5 ± 6.3	66.3 ± 6.3	75.4 ± 7.8	10.8 ± 3.2	$2.81^{+0.63}_{-0.68}$	$13.22^{+0.15}_{-0.20}$
HerMES J233927.1−052258	HELMS_RED_180	51.4 ± 6.1	59.4 ± 5.9	66.9 ± 7.9	18.1 ± 4.3	$3.21^{+0.71}_{-0.76}$	$13.33^{+0.14}_{-0.19}$
HerMES J004120.1+015220	HELMS_RED_183	44.4 ± 6.0	65.3 ± 6.4	67.5 ± 7.2	21.5 ± 3.6	$3.63^{+0.64}_{-0.63}$	$13.41^{+0.10}_{-0.14}$
HerMES J235818.3−081029	HELMS_RED_188	45.8 ± 5.5	76.4 ± 5.6	77.0 ± 6.5	26.9 ± 5.6	$3.85^{+0.62}_{-0.60}$	$13.51^{+0.10}_{-0.12}$
HerMES J010733.0+042228	HELMS_RED_191	46.1 ± 6.1	69.3 ± 5.7	80.7 ± 8.1	15.7 ± 4.3	$3.55^{+0.61}_{-0.61}$	$13.38^{+0.11}_{-0.13}$
HerMES J003846.3−033526	HELMS_RED_196	54.7 ± 5.9	63.4 ± 5.7	68.5 ± 6.6	16.3 ± 3.4	$3.16^{+0.66}_{-0.67}$	$13.32^{+0.13}_{-0.17}$
HerMES J235320.4−054743	HELMS_RED_202	35.3 ± 5.7	49.6 ± 6.3	66.3 ± 7.6	13.7 ± 4.5	$3.69^{+0.69}_{-0.66}$	$13.31^{+0.12}_{-0.15}$
HerMES J232711.4−051505	HELMS_RED_206	57.2 ± 6.0	64.8 ± 6.2	75.4 ± 6.8	11.7 ± 4.2	$3.09^{+0.63}_{-0.62}$	$13.29^{+0.12}_{-0.17}$
HerMES J010510.0+044223	HELMS_RED_212	41.3 ± 6.5	54.5 ± 5.8	72.0 ± 7.5	27.5 ± 4.3	$3.91^{+0.72}_{-0.70}$	$13.48^{+0.12}_{-0.14}$
HerMES J001134.9+002738	HELMS_RED_219	46.9 ± 5.6	69.4 ± 6.2	69.7 ± 6.4	23.4 ± 4.4	$3.66^{+0.63}_{-0.61}$	$13.44^{+0.11}_{-0.13}$
HerMES J234106.3−061457	HELMS_RED_223	56.5 ± 6.7	76.7 ± 6.4	83.3 ± 7.3	17.8 ± 4.2	$3.40^{+0.59}_{-0.59}$	$13.41^{+0.11}_{-0.14}$
HerMES J235900.9−062939	HELMS_RED_224	48.2 ± 5.7	54.9 ± 6.2	67.0 ± 7.1	14.9 ± 4.0	$3.24^{+0.69}_{-0.72}$	$13.29^{+0.14}_{-0.19}$
HerMES J235647.0−023312	HELMS_RED_226	29.6 ± 5.7	58.3 ± 5.5	69.2 ± 7.6	20.9 ± 5.1	$4.16^{+0.67}_{-0.69}$	$13.44^{+0.10}_{-0.13}$
HerMES J233838.8+000032	HELMS_RED_228	58.4 ± 5.9	61.9 ± 5.8	67.7 ± 6.9	10.6 ± 3.4	$2.84^{+0.65}_{-0.71}$	$13.21^{+0.15}_{-0.21}$
HerMES J002012.1−044523	HELMS_RED_232	44.0 ± 6.2	57.9 ± 6.2	67.4 ± 7.1	20.4 ± 4.1	$3.58^{+0.68}_{-0.67}$	$13.39^{+0.11}_{-0.15}$
HerMES J234707.6+021633	HELMS_RED_235	55.7 ± 6.4	59.4 ± 6.2	67.5 ± 6.6	23.4 ± 3.5	$3.15^{+0.72}_{-0.74}$	$13.37^{+0.14}_{-0.20}$
HerMES J233123.5+000631	HELMS_RED_241	60.3 ± 6.4	71.2 ± 6.8	71.5 ± 7.1	14.3 ± 4.5	$3.08^{+0.63}_{-0.64}$	$13.32^{+0.12}_{-0.17}$
HerMES J234247.3−024555	HELMS_RED_242	60.0 ± 6.6	80.7 ± 5.9	81.0 ± 7.6	13.3 ± 4.6	$3.22^{+0.58}_{-0.59}$	$13.37^{+0.12}_{-0.14}$
HerMES J235512.7−045840	HELMS_RED_249	39.1 ± 5.9	69.2 ± 6.5	73.3 ± 7.7	17.8 ± 4.8	$3.79^{+0.61}_{-0.65}$	$13.41^{+0.10}_{-0.13}$
HerMES J002057.1+051242	HELMS_RED_251	42.5 ± 6.1	46.0 ± 6.0	65.4 ± 7.0	16.4 ± 3.7	$3.37^{+0.75}_{-0.80}$	$13.30^{+0.14}_{-0.20}$
HerMES J003743.6−011423	HELMS_RED_255	48.0 ± 6.2	53.1 ± 5.9	64.4 ± 7.4	16.8 ± 3.4	$3.20^{+0.73}_{-0.80}$	$13.29^{+0.15}_{-0.21}$
HerMES J001618.9−040118	HELMS_RED_258	48.7 ± 6.3	68.0 ± 6.1	90.6 ± 7.1	11.4 ± 4.4	$3.44^{+0.59}_{-0.61}$	$13.36^{+0.11}_{-0.14}$
HerMES J001936.8+025855	HELMS_RED_262	51.6 ± 5.9	63.7 ± 6.3	67.3 ± 7.3	16.6 ± 3.6	$3.26^{+0.64}_{-0.66}$	$13.33^{+0.13}_{-0.16}$
HerMES J005557.4+063518	HELMS_RED_264	54.6 ± 6.5	61.7 ± 6.3	73.5 ± 7.3	6.8 ± 6.1	$3.11^{+0.67}_{-0.67}$	$13.28^{+0.14}_{-0.17}$
HerMES J000831.4+035303	HELMS_RED_266	44.6 ± 6.3	65.7 ± 5.5	69.9 ± 7.1	11.0 ± 3.2	$3.29^{+0.58}_{-0.61}$	$13.27^{+0.11}_{-0.14}$
HerMES J001732.5+031559	HELMS_RED_267	46.5 ± 5.9	59.2 ± 5.8	64.6 ± 8.2	17.5 ± 3.7	$3.35^{+0.68}_{-0.69}$	$13.33^{+0.13}_{-0.17}$
HerMES J004919.4+012439	HELMS_RED_268	53.9 ± 6.2	54.4 ± 6.1	69.7 ± 6.7	21.3 ± 5.7	$3.16^{+0.75}_{-0.79}$	$13.36^{+0.15}_{-0.21}$
HerMES J234220.9−045604	HELMS_RED_269	50.9 ± 6.4	55.3 ± 5.9	67.1 ± 6.8	26.8 ± 4.5	$3.39^{+0.74}_{-0.75}$	$13.41^{+0.14}_{-0.18}$
HerMES J235830.9+005631	HELMS_RED_270	47.8 ± 5.7	62.3 ± 5.8	63.8 ± 7.0	31.5 ± 4.8	$3.64^{+0.72}_{-0.69}$	$13.47^{+0.12}_{-0.15}$
HerMES J003819.5+064505	HELMS_RED_272	47.7 ± 5.8	61.5 ± 6.0	64.4 ± 6.5	13.7 ± 3.9	$3.29^{+0.63}_{-0.62}$	$13.29^{+0.12}_{-0.16}$
HerMES J002943.2+010330	HELMS_RED_277	53.0 ± 5.8	63.7 ± 6.3	67.3 ± 8.0	17.6 ± 3.6	$3.20^{+0.67}_{-0.70}$	$13.33^{+0.13}_{-0.18}$
HerMES J010231.1+005416	HELMS_RED_279	55.1 ± 6.3	61.6 ± 6.2	83.2 ± 7.5	10.5 ± 4.6	$3.16^{+0.65}_{-0.64}$	$13.30^{+0.13}_{-0.17}$
HerMES J232606.3−023610	HELMS_RED_283	34.6 ± 6.8	61.5 ± 5.8	65.6 ± 7.6	11.4 ± 4.6	$3.63^{+0.63}_{-0.68}$	$13.32^{+0.10}_{-0.15}$
HerMES J004811.1+000810	HELMS_RED_287	47.9 ± 6.1	48.6 ± 6.4	63.8 ± 6.9	18.4 ± 4.1	$3.17^{+0.76}_{-0.82}$	$13.30^{+0.16}_{-0.21}$
HerMES J234046.8−051205	HELMS_RED_288	38.5 ± 6.7	44.9 ± 6.3	67.9 ± 7.2	16.8 ± 4.3	$3.65^{+0.76}_{-0.76}$	$13.33^{+0.13}_{-0.16}$
HerMES J002625.4+024405	HELMS_RED_290	31.3 ± 6.3	56.7 ± 6.1	65.8 ± 7.2	16.6 ± 3.7	$3.88^{+0.65}_{-0.68}$	$13.36^{+0.10}_{-0.14}$
HerMES J002148.7+013522	HELMS_RED_293	30.8 ± 6.1	58.1 ± 5.9	68.5 ± 7.1	15.4 ± 3.9	$3.89^{+0.63}_{-0.69}$	$13.36^{+0.10}_{-0.14}$
HerMES J233159.8−025408	HELMS_RED_301	26.6 ± 7.2	48.4 ± 6.2	64.5 ± 7.2	18.2 ± 4.5	$4.14^{+0.74}_{-0.72}$	$13.39^{+0.11}_{-0.14}$
HerMES J003706.2+011634	HELMS_RED_309	31.8 ± 5.9	63.5 ± 6.3	70.3 ± 7.0	21.8 ± 3.6	$4.07^{+0.63}_{-0.67}$	$13.45^{+0.10}_{-0.12}$
HerMES J010151.9+000822	HELMS_RED_314	42.1 ± 6.4	68.4 ± 6.5	69.5 ± 6.7	21.2 ± 5.3	$3.78^{+0.64}_{-0.63}$	$13.43^{+0.10}_{-0.13}$
HerMES J004808.8+040359	HELMS_RED_315	47.4 ± 5.8	65.3 ± 5.8	66.4 ± 7.1	13.5 ± 4.3	$3.34^{+0.62}_{-0.61}$	$13.31^{+0.11}_{-0.14}$
HerMES J000154.4−031845	HELMS_RED_318	33.0 ± 5.4	47.5 ± 5.6	64.4 ± 7.0	8.7 ± 4.5	$3.58^{+0.68}_{-0.67}$	$13.24^{+0.11}_{-0.15}$
HerMES J232656.9−043112	HELMS_RED_319	33.6 ± 6.6	42.5 ± 6.1	63.6 ± 7.7	20.7 ± 4.6	$3.95^{+0.80}_{-0.79}$	$13.38^{+0.12}_{-0.16}$

Table A1 – *continued*

Source name	Name	S_{250} (mJy)	S_{350} (mJy)	S_{500} (mJy)	S_{850} (mJy)	phot-z	$\log(L_{\mathrm{FIR}}/L_{\odot})$
HerMES J232658.4−021900	HELMS_RED_320	60.5 ± 6.2	60.9 ± 6.0	77.1 ± 7.1	16.3 ± 4.8	$3.01^{+0.71}_{-0.82}$	$13.33^{+0.15}_{-0.23}$
HerMES J003527.5+002227	HELMS_RED_323	51.2 ± 5.8	61.8 ± 6.2	70.3 ± 7.1	27.3 ± 5.8	$3.51^{+0.68}_{-0.73}$	$13.45^{+0.13}_{-0.16}$
HerMES J232856.6−041652	HELMS_RED_324	75.5 ± 6.3	80.0 ± 5.8	80.6 ± 6.8	22.4 ± 4.5	$2.92^{+0.67}_{-0.76}$	$13.41^{+0.15}_{-0.22}$
HerMES J234656.1+002246	HELMS_RED_326	36.3 ± 5.9	58.1 ± 5.9	67.8 ± 7.4	25.0 ± 3.7	$4.00^{+0.68}_{-0.64}$	$13.46^{+0.11}_{-0.12}$
HerMES J233254.7−060301	HELMS_RED_331	42.1 ± 7.4	60.0 ± 5.6	64.0 ± 8.5	10.7 ± 4.7	$3.35^{+0.66}_{-0.67}$	$13.28^{+0.12}_{-0.16}$
HerMES J232414.9−025250	HELMS_RED_333	67.4 ± 5.5	70.8 ± 6.0	74.3 ± 7.2	20.4 ± 4.8	$2.91^{+0.68}_{-0.77}$	$13.36^{+0.15}_{-0.22}$
HerMES J232057.2−044412	HELMS_RED_335	50.9 ± 6.4	63.8 ± 6.2	70.0 ± 7.1	23.7 ± 5.1	$3.47^{+0.68}_{-0.70}$	$13.43^{+0.13}_{-0.16}$
HerMES J001242.5−042634	HELMS_RED_336	53.8 ± 5.9	57.4 ± 5.8	64.4 ± 6.6	9.1 ± 3.6	$2.87^{+0.68}_{-0.72}$	$13.18^{+0.16}_{-0.21}$
HerMES J005008.5+024618	HELMS_RED_339	52.1 ± 6.3	55.6 ± 5.8	64.5 ± 8.1	19.7 ± 4.9	$3.10^{+0.75}_{-0.80}$	$13.32^{+0.15}_{-0.22}$
HerMES J003306.4+030116	HELMS_RED_342	39.5 ± 6.0	53.4 ± 5.9	68.2 ± 7.0	8.7 ± 4.5	$3.41^{+0.66}_{-0.64}$	$13.25^{+0.12}_{-0.15}$
HerMES J235955.2−032724	HELMS_RED_348	44.5 ± 5.6	50.4 ± 5.9	68.4 ± 6.4	10.8 ± 3.8	$3.25^{+0.67}_{-0.66}$	$13.24^{+0.13}_{-0.16}$
HerMES J000742.7+051438	HELMS_RED_350	49.7 ± 5.7	59.4 ± 5.8	65.1 ± 6.8	12.4 ± 3.3	$3.13^{+0.64}_{-0.63}$	$13.57^{+0.12}_{-0.17}$
HerMES J002223.9+025047	HELMS_RED_353	31.6 ± 6.0	46.7 ± 6.5	65.8 ± 7.2	24.1 ± 4.1	$4.15^{+0.75}_{-0.69}$	$13.25^{+0.11}_{-0.13}$
HerMES J003446.0+045549	HELMS_RED_368	44.6 ± 6.4	55.4 ± 6.2	74.0 ± 7.5	24.4 ± 3.7	$3.71^{+0.69}_{-0.70}$	$13.44^{+0.12}_{-0.15}$
HerMES J234723.5−015213	HELMS_RED_369	41.7 ± 5.5	49.1 ± 5.8	63.4 ± 7.1	18.0 ± 4.7	$3.47^{+0.72}_{-0.75}$	$13.44^{+0.14}_{-0.18}$
HerMES J003931.4+014822	HELMS_RED_373	53.6 ± 5.9	70.6 ± 6.2	79.7 ± 7.5	18.5 ± 3.7	$3.42^{+0.61}_{-0.58}$	$13.33^{+0.12}_{-0.13}$
HerMES J005016.4+055923	HELMS_RED_377	51.5 ± 5.6	61.8 ± 6.5	71.0 ± 7.2	24.1 ± 4.7	$3.43^{+0.67}_{-0.71}$	$13.39^{+0.12}_{-0.18}$
HerMES J233755.0−051000	HELMS_RED_379	60.3 ± 6.5	82.0 ± 6.3	85.3 ± 7.8	19.6 ± 4.9	$3.40^{+0.59}_{-0.58}$	$13.42^{+0.11}_{-0.14}$
HerMES J232933.2+003149	HELMS_RED_385	26.7 ± 5.7	34.8 ± 6.1	68.7 ± 7.5	15.6 ± 4.5	$4.11^{+0.81}_{-0.73}$	$13.44^{+0.12}_{-0.13}$
HerMES J232101.9−033260	HELMS_RED_387	37.5 ± 5.9	49.5 ± 5.9	64.6 ± 6.9	11.5 ± 4.8	$3.56^{+0.69}_{-0.67}$	$13.34^{+0.12}_{-0.14}$
HerMES J001016.5−032131	HELMS_RED_389	40.8 ± 6.1	61.3 ± 6.0	65.0 ± 7.2	20.0 ± 3.7	$3.68^{+0.65}_{-0.64}$	$13.28^{+0.11}_{-0.14}$
HerMES J235712.3+022917	HELMS_RED_390	47.0 ± 6.3	55.0 ± 6.3	68.0 ± 7.9	19.5 ± 5.1	$3.42^{+0.72}_{-0.77}$	$13.39^{+0.14}_{-0.18}$
HerMES J001251.7+061210	HELMS_RED_399	78.2 ± 5.8	79.6 ± 6.4	81.8 ± 6.6	23.3 ± 4.4	$2.85^{+0.67}_{-0.75}$	$13.36^{+0.15}_{-0.23}$
HerMES J234602.1+001736	HELMS_RED_402	46.9 ± 6.6	48.1 ± 6.2	64.6 ± 7.2	18.9 ± 3.4	$3.25^{+0.76}_{-0.83}$	$13.41^{+0.14}_{-0.22}$
HerMES J010735.0+032259	HELMS_RED_403	49.1 ± 6.7	52.8 ± 6.1	64.1 ± 7.7	15.0 ± 5.4	$3.14^{+0.77}_{-0.86}$	$13.31^{+0.15}_{-0.23}$
HerMES J234612.3−054812	HELMS_RED_405	23.0 ± 5.5	47.6 ± 6.0	64.2 ± 8.1	8.7 ± 4.6	$3.91^{+0.68}_{-0.75}$	$13.28^{+0.11}_{-0.15}$
HerMES J004414.7+002550	HELMS_RED_420	27.4 ± 6.0	55.6 ± 5.9	68.5 ± 7.6	16.2 ± 3.6	$3.99^{+0.64}_{-0.70}$	$13.27^{+0.10}_{-0.13}$
HerMES J000127.4−010614	HELMS_RED_421	65.4 ± 6.3	69.1 ± 5.9	72.5 ± 7.3	18.5 ± 4.8	$2.93^{+0.70}_{-0.79}$	$13.37^{+0.15}_{-0.23}$
HerMES J004055.2+021131	HELMS_RED_423	45.7 ± 6.1	57.5 ± 5.9	66.0 ± 7.1	22.1 ± 3.5	$3.52^{+0.69}_{-0.71}$	$13.34^{+0.13}_{-0.16}$
HerMES J003136.0−011856	HELMS_RED_428	39.9 ± 6.0	52.6 ± 6.0	64.5 ± 6.4	14.9 ± 4.1	$3.54^{+0.68}_{-0.65}$	$13.39^{+0.12}_{-0.14}$
HerMES J002414.5+035239	HELMS_RED_430	47.8 ± 6.1	52.1 ± 6.3	64.9 ± 7.2	12.1 ± 3.8	$3.09^{+0.72}_{-0.77}$	$13.32^{+0.14}_{-0.22}$
HerMES J233857.1−034441	HELMS_RED_434	59.2 ± 5.6	65.1 ± 5.8	65.7 ± 7.0	16.4 ± 4.4	$2.97^{+0.69}_{-0.76}$	$13.23^{+0.15}_{-0.22}$
HerMES J002000.9−060219	HELMS_RED_440	49.4 ± 6.2	71.7 ± 5.8	76.9 ± 7.2	10.0 ± 4.3	$3.29^{+0.59}_{-0.60}$	$13.30^{+0.12}_{-0.14}$
HerMES J232909.1+003450	HELMS_RED_441	38.0 ± 6.4	50.6 ± 5.9	76.0 ± 7.9	20.2 ± 3.3	$3.83^{+0.71}_{-0.66}$	$13.32^{+0.11}_{-0.14}$
HerMES J232249.3−024437	HELMS_RED_443	52.1 ± 5.9	54.8 ± 6.3	66.9 ± 7.4	21.0 ± 4.7	$3.17^{+0.73}_{-0.78}$	$13.40^{+0.15}_{-0.20}$
HerMES J002824.0−013329	HELMS_RED_447	47.2 ± 5.5	60.1 ± 5.8	69.5 ± 6.6	14.0 ± 3.9	$3.34^{+0.63}_{-0.61}$	$13.34^{+0.11}_{-0.14}$
HerMES J000823.4+012423	HELMS_RED_448	43.7 ± 6.2	58.1 ± 6.7	63.9 ± 6.6	12.5 ± 3.3	$3.32^{+0.63}_{-0.62}$	$13.31^{+0.13}_{-0.14}$
HerMES J234547.9−054412	HELMS_RED_449	52.0 ± 6.7	59.4 ± 6.2	70.7 ± 7.7	19.4 ± 5.2	$3.30^{+0.73}_{-0.78}$	$13.26^{+0.14}_{-0.20}$
HerMES J232619.7−050855	HELMS_RED_451	49.2 ± 6.5	61.3 ± 6.4	65.3 ± 8.1	20.0 ± 4.6	$3.36^{+0.70}_{-0.73}$	$13.37^{+0.13}_{-0.17}$
HerMES J003753.1+050029	HELMS_RED_452	47.5 ± 7.1	61.5 ± 6.0	68.2 ± 7.2	12.1 ± 3.4	$3.22^{+0.63}_{-0.63}$	$13.36^{+0.13}_{-0.17}$
HerMES J233351.1−035745	HELMS_RED_458	54.9 ± 6.2	61.3 ± 6.3	79.6 ± 7.1	8.0 ± 4.7	$3.09^{+0.64}_{-0.63}$	$13.26^{+0.13}_{-0.17}$
HerMES J001638.5+042328	HELMS_RED_463	31.8 ± 6.2	46.5 ± 6.3	63.5 ± 6.8	12.0 ± 3.7	$3.68^{+0.69}_{-0.68}$	$13.27^{+0.11}_{-0.15}$
HerMES J010438.2+002613	HELMS_RED_472	42.4 ± 6.0	55.8 ± 6.3	64.7 ± 7.1	16.9 ± 3.8	$3.51^{+0.68}_{-0.66}$	$13.27^{+0.13}_{-0.15}$

[1]*Astronomy Centre, Department of Physics and Astronomy, University of Sussex, Brighton BN1 9QH, UK*

[2]*Astrophysics Group, Imperial College, Blackett Laboratory, Prince Consort Road, London SW7 2AZ, UK*

[3]*Department of Astronomy, Cornell University, Space Sciences Building, Ithaca, NY 14853, USA*

[4]*Aix-Marseille Universite, CNRS, LAM (Laboratoire d Astrophysique de Marseille) UMR 7326, F-13388 Marseille, France*

[5]*Department of Physics and Atmospheric Science, Dalhousie University, Halifax, NS B3H 4R2, Canada*

[6]*Department of Physics & Astronomy, University of California, Irvine, CA 92697, USA*

[7]*Centre for Astrophysics Research, University of Hertfordshire, Hatfield AL10 9AB, UK*

[8]*Instituto de Astrofisica de Canarias (IAC), E-38205 La Laguna, Tenerife, Spain*

[9]*Dpto. Astrofíisica, Universidad de La Laguna, E-38206 La Laguna, Tenerife, Spain*

[10]*INAF-Osservatorio Astronomico di Padova, Vicolo dell Osservatorio 5, I-35122 Padova, Italy*

[11]*Institute for Astronomy, University of Edinburgh, Royal Observatory, Edinburgh EH9 3HJ, UK*

[12]*School of Physics & Astronomy, Cardiff University, Queen's Buildings, The Parade, Cardiff CF24 3AA, UK*

[13]*School of Sciences, European University Cyprus, Diogenes Street, Engomi, 1516 Nicosia, Cyprus*

[14]*Department of Physics, Virginia Tech, Blacksburg, VA 24061, USA*

[15]*UK Astronomy Technology Centre, Royal Observatory, Blackford Hill, Edinburgh EH9 3HJ, UK*

[16]*European Southern Observatory, Karl-Schwarzschild-Straße 2, D-85748 Garching, Germany*

[17]*Department of Astronomy, University of Cape Town, Private Bag X3, Rondebosch 7701, South Africa*

[18]*Department of Physics and Astronomy, University of the Western Cape, Robert Sobukwe Road, 7535 Bellville, Cape Town, South Africa*

[19]*INAF – Istituto di Radioastronomia, via Gobetti 101, I-40129 Bologna, Italy*

[20]*Harvard-Smithsonian Center for Astrophysics, Cambridge, MA 02138, UK*

[21]*Department of Physics and Astronomy, University of British Columbia, 6224 Agricultural Road, Vancouver, BC V6T-1Z1, Canada*

[22]*Mullard Space Science Laboratory, University College London, Holmbury St. Mary, Dorking, Surrey RH5 6NT, UK*

[23]*Department of Astronomy, Department of Physics, University of Illinois, 1002 West Green St, Urbana, IL 61801, USA*

[24]*SRON Netherlands Institute for Space Research, Landleven 12, NL-9747 AD, Groningen, the Netherlands*

[25]*Kapteyn Astronomical Institute, University of Groningen, Postbus 800, NL-9700 AV, Groningen, the Netherlands*

[26]*Centre for Extragalactic Astronomy, Department of Physics, Durham University, South Road, Durham DH1 3LE, UK*

[27]*Center for Detectors, School of Physics and Astronomy, Rochester Institute of Technology, Rochester, NY 14623, USA*

This paper has been typeset from a TEX/LATEX file prepared by the author.